Toward constraining regional-scale fluxes of CO2 with atmospheric observations over a continent: 2. Analysis of COBRA data using a receptor-oriented framework

Article *in* Journal of Geophysical Research Atmospheres · December 2003

DOI: 10.1029/2003JD003770

CITATIONS
287

READS
117

8 authors, including:

John C. Lin
University of Utah
157 PUBLICATIONS **4,151** CITATIONS
SEE PROFILE

Steven C. Wofsy
Harvard University
635 PUBLICATIONS **64,106** CITATIONS
SEE PROFILE

Bruce C. Daube
Harvard University
158 PUBLICATIONS **14,016** CITATIONS
SEE PROFILE

Arlyn Elizabeth Andrews
National Oceanic and Atmospheric Administration
196 PUBLICATIONS **8,233** CITATIONS
SEE PROFILE

Constraining regional to continental scale fluxes of CO_2 with atmospheric observations over a continent: A receptor-oriented analysis of COBRA data

C. Gerbig, J. C. Lin, S. C. Wofsy, B. C. Daube, and A. E. Andrews[1]

Dept. of Earth and Planetary Sciences and Division of Engineering and Applied Sciences, Harvard University, Cambridge, MA

B. B. Stephens[2] and P. S. Bakwin

Climate Monitoring and Diagnostic Laboratory, National Oceanic and Atmospheric Administration, Boulder, CO

C. A. Grainger

Dept. of Atmospheric Sciences, University of North Dakota, Grand Forks, ND

Manuscript version: Friday, October 04, 2002

Abstract. We analyze observations of CO_2 and CO over North America acquired during the CO_2 Budget and Rectification Airborne (COBRA) study in 2000. The COBRA dataset is unique in its dense spatial coverage and extensive profiling in the lower atmosphere. Statistical analyses indicate that CO_2 mixed layer averages can be determined from vertical profiles with an accuracy limited by atmospheric variance to ±0.2 ppm. The data show that models require horizontal resolution of smaller than 30 km to fully resolve spatial variations of atmospheric CO_2 near the earth's surface and to avoid inaccuracies due to representativeness error.

Strong signatures of land surface fluxes were observed in the active and relic mixed layers of the atmosphere. We present a "receptor-oriented" analysis framework to quantitatively link concentrations at measurement locations (receptors) to surface fluxes in upwind regions. The analysis incorporates two main components: 1) the Stochastic Time-Inverted Lagrangian Transport (STILT) model, driven with assimilated winds and running backward in time to map out the source-receptor relationship (footprint) at high temporal and spatial resolution, and 2) a parameterization for biosphere-atmosphere fluxes, derived from the AmeriFlux network of eddy covariance measurements, that serves as a "first-guess" for fluxes. Combining these components with an observation-based lateral boundary condition for CO_2 allows quantitative comparison between the top-down constraint on fluxes from airborne observations of CO_2, with the bottom-up constraint of eddy flux measurements. Discrepancies between simulated and observed CO_2 distributions are assessed to indicate where improvements are needed, including representation of biosphere-atmosphere fluxes and convective processes in atmospheric transport.

1. Introduction

Projections of future atmospheric concentrations of CO_2 represent a major uncertainty in predicting future climate. A critical prerequisite for understanding the distribution of carbon sources and sinks over the globe and their responses to climate and environmental forcing is the capability to quantify regional to continental scale (10^2~10^3 km) sources/sinks from atmospheric data. Methods for quantifying the source/sink distribution will also be needed to verify compliance with CO_2 reduction protocols or "carbon trading", should they come into effect.

Atmospheric CO_2 measurements have played a key role in assessing source/sink distributions on global scales, using inter-hemispheric differences [*Conway et al.*, 1994], and more recently, quantifying continental/ocean basin scale fluxes by using information contained in zonal gradients [e.g. *Fan et al.*, 1998]. A common method to infer sources and sinks from atmospheric measurements is to use a global tracer transport model to establish a relationship between fluxes and tracer distributions, and then to derive source estimates using inverse techniques [e.g., *Bousquet et al.*, 1999; *Fan et al.*, 1998; *Tans et al.*, 1990]. Estimates of CO_2 fluxes from inversion of global CO_2 measurements are affected by a variety of limitations even at continental scales: (1) Most inverse studies use data collected at stations remote from the terrestrial biosphere, which are deliberately located to be insensitive to the continental fluxes on regional scales [*Gloor et al.*, 2000]; Monthly mean concentrations are usually used, and "high frequency variations" caused by weather systems are regarded as noise [*Gloor et al.*, 1999]. (2) Point measurements are difficult to represent in transport models with large grid cells. These temporal and spatial mismatches lead to "*representativeness errors*"; (3) Solving for fluxes aggregated over large regions is problematic if the measurements used in the inversion are not evenly

influenced by the whole region ("*aggregation error*") [*Kaminski et al.*, 2001]; (4) covariances between mixed layer height and biosphere-atmosphere exchange fluxes [*Denning et al.*, 1996] are usually not properly represented in models, causing biases over diurnal or seasonal time scales (*"rectification errors"*).

The North American Carbon Program (NACP) [*Wofsy and Harris*, 2002], an inter-agency effort to address the role of North America in the global carbon cycle, has recently outlined a strategy for developing the scientific capability to determine net fluxes of CO_2 on regional and continental scales. The NACP plan proposed a network of ground based, airborne, and spaceborne observations of CO_2 mixing ratios over the continents, to address the limitations noted above in order to determine the terrestrial fluxes of CO_2 that most strongly affect atmospheric concentration.

The NACP envisioned a modeling framework capable of assimilating these observations, termed "model-data fusion". Continental CO_2 measurements, such as made from tall towers [e.g., *Bakwin et al.*, 1995; *Bakwin et al.*, 1998; *Haszpra et al.*, 2001], cannot be utilized optimally by current-generation analysis frameworks. Continental CO_2 fluxes exhibit strong spatial and temporal variations: biospheric fluxes reverse sign between night (respiration) and day (respiration + photosynthetic uptake). The atmosphere modifies the signals from these variable sources and sinks, causing a CO_2 distribution which varies significantly on relatively small spatial and temporal scales, greatly enhancing *representativeness errors*. The proximity of measurements to strong surface fluxes requires an analysis framework that resolves sources and sinks in the near field of the observations [*Lin et al.*, 2002], even if large-scale fluxes are the objective; otherwise *aggregation errors* may invalidate the flux estimates. The covariance between

atmospheric mixing and fluxes on diurnal time scales ("*diurnal rectifier effect*") needs to be accurately represented. Models with high temporal and spatial resolution are required, and methods must be developed to use these models to interpret complex datasets and derive large-scale fluxes.

A simple approach to quantify fluxes from atmospheric measurements is to compute mass budgets in a one-dimensional conceptual framework. For example, the boundary layer budget technique has been applied to vertical profiles of CO_2, measured at the same location at different times [*Denmead et al.*, 1996; *Kuck et al.*, 2000]. However, one-dimensional frameworks cannot account for advection of air from different upstream areas at different times. A pseudo-Lagrangian framework was used by *Chou et al.* [2002] to infer basin scale biosphere-atmosphere exchange fluxes from differences between CO_2 profiles over the Atlantic (upwind) and over the Amazon Basin, collected at multiple times per day over several weeks. The framework required surface fluxes that did not vary strongly with location over the Basin, and an ensemble of transport paths sampling the same general area over the measurement period. These simplifying conditions cannot be expected over North America. Frontal systems cause transport paths to change drastically on synoptic time scales, and fluxes may change significantly with location due to differences in vegetation type and to the north/south migration of seasonal changes.

This paper introduces an analysis framework for quantifying fluxes on regional to continental scales, intended to address the specific problems encountered when using data collected over the continent, inlcuding *representativeness* and *aggregation errors* and the *diurnal rectifier*. The framework outlined in Fig. 1 consists of two main components: a receptor-oriented transport model and a biospheric flux model with high spatial and

temporal resolution. The framework is designed to take as input multiple data streams and provide as output optimal biospheric parameters and their associated regional fluxes. We present a first application of the framework to aircraft CO_2 and AmeriFlux observations. The receptor-oriented Stochastic Time-Inverted Lagrangian Transport (STILT) model [*Lin et al.*, 2002] calculates upstream influences for a point observation (receptor) with assimilated winds from a mesoscale model. An ensemble of particles is released at the receptor (measurement location) and transported backwards in time by mean and turbulent winds; the particle density maps out upstream influences. The resulting influence functions are equivalent to the adjoint of the transport model, in that they represent sensitivities of atmospheric concentrations to changes in surface fluxes or upstream boundary values. Biospheric fluxes are calculated with a simple biosphere model that uses temperature and radiation from assimilated meteorological data. Responses to these meteorological drivers are keyed to data from eddy covariance flux towers in the AmeriFlux network [*Baldocchi and al.*, 2001]. Land cover is derived from the IGBP 1-km resolution vegetation data [*Belward et al.*, 1999].

The data analysis framework allows estimating regional fluxes from the observed CO_2 distributions in several steps (Fig. 1): (1) Influence functions are calculated for the measurement locations using STILT. (2) These influences are coupled to a CO_2 emission inventory and to a CO_2 background field to derive the *fossil fuel CO_2 signal* and the *advected background CO_2*. (3) A measurement-based *CO_2 vegetation signal* is calculated as the difference between measured CO_2 and the sum of advected CO_2 and fossil fuel CO_2 signal. (4) Modeled CO_2 vegetation signals are derived by coupling the influence functions to the biosphere model. (5) The parameters of the biosphere model are

optimized to obtain a match between modeled and measured CO_2 vegetation signals. (6) Regional fluxes are derived by driving the optimized biosphere flux model with observed meteorological conditions.

The aircraft data used as input to the analysis framework were collected during the *CO_2 Budget and Rectification Airborne Study* (COBRA-2000) during August 2000. COBRA-2000 was designed as a pilot study to determine the characteristics of the atmospheric CO_2 signal from terrestrial ecosystem processes over North America and to test concepts to quantify sources and sinks from those signals [*Stephens et al.*, 1999]. The dense spatial coverage and multiple profiles in COBRA-2000 observations provide a snapshot of data that can be collected by future sampling networks or satellites, providing a test data set for diagnostic models designed to infer regional and continental scale fluxes.

We start in section 2 with a statistical analysis of COBRA data to examine the spatial variability in CO_2, highlighting the resolution required for a transport model to resolve observed variability. In section 3 we describe the major elements of the data analysis framework designed to cope with, and learn from, the observed variability, including a statistical model used to create the lateral boundary condition for CO_2 and CO from ground-based and airborne measurements to the west of the North American continent. Investigation of sensitivities of the transport model to key parameters is presented in section 4.

The results of applying the receptor-oriented framework to COBRA data are discussed in section 5, with a presentation of the surface influence functions ("footprints") for COBRA (section 5.1), the derivation of the measurement-based

vegetation signal (section 5.2), and the optimization of the biosphere model and regional flux estimates (section 5.3). In section 6, we relate discrepancies between the observed and modeled vegetation signals to specific shortcomings of available meteorological data and other elements of the framework.

2. Measurements in COBRA-2000

Approximately 30 flight legs were conducted as part of COBRA over the U.S. and southern Canada during August, 2000, with frequent vertical profiles from ~300 m to 10 km above ground, emphasizing the planetary boundary-layer (PBL). We used the University of North Dakota Cessna Citation-2, a small, straight-wing twin-engine fan-jet that can take off from relatively short airstrips and fly for significant distances in the PBL, at speeds as low as ~72 m/s. The Citation can also cover long distances (cruise at > 300 kts), and can profile as high as 12 km altitude.

Measurements of CO_2 were made using a high accuracy sensor flown previously on stratospheric balloons [*Daube et al.*, 2002], with a water trap added. In-flight calibrations were carried out every 20 minutes using standards traceable to the WMO Central CO_2 Laboratory [*Zhao et al.*, 1997] to an accuracy of 0.1ppm, and a zero measurement was done every 10 minutes. The precision of 0.25 ppm (2-σ) for the tropospheric measurements was somewhat poorer than achieved in the balloon configuration due to marginal performance of a solenoid valve. Data were recorded at 4 Hz and reported at 0.5 Hz, representing the median of eight measurements.

Measurements of CO were conducted using a modified commercial instrument (AL5001, Aero-Laser GmbH, Germany), based on the Vacuum-Ultraviolet (VUV) fluorescence technique, with a precision of 2 ppbv and a long-term accuracy of 3 ppb

[*Gerbig et al.*, 1996; *Gerbig et al.*, 1999]. Modifications included substituting the drier assembly as described in *Gerbig et al.* [1999], which improved stability of the zero signal significantly. The instrument sampled at 1 Hz and was automatically calibrated and zeroed at 30-minute intervals in flight using a standard gas mixture traceable to NOAA CMDL [*Novelli et al.*, 1992]. An identical VUV instrument showed excellent agreement with a tunable diode laser sensor in an airborne inter-comparison [*Holloway et al.*, 2000].

Standard equipment was used for meteorological parameters: Dew point was measured with a cooled mirror hygrometer (EG&G, Model 137), a Rosemount sensor (102 Probe) was used for temperature, and static pressure was measured with a Rosemount transducer (1201F1).

COBRA flights (Fig. 2) were conducted on two spatial scales: (1) Regional (~10^4 km^2) flights with multiple characterizations of the same airmass at different times were conducted to constrain fluxes at selected locations in North Dakota, in Wisconsin (near the WLEF tall tower), and in Maine, near the Howland Forest AmeriFlux site. These flights numbered 15 with about 100 vertical soundings covering 0.3-3 km above ground level (AGL). (2) Trans-continental surveys (10 flight segments, Table 1) accounted for about 40 vertical profiles. This paper focuses primarily on CO_2 and CO measurements from the transcontinental surveys, except all data were used in the statistical analysis of representativeness error (section 2.2).

2.1. Observed distributions of CO_2 and CO

Two trans-continental surveys (Fig. 2 and Table 1) covered the northern tier of the U.S. from Maine to North Dakota and the southern tier starting from Idaho and sweeping through Colorado, Kansas, the central Midwest, and north to Maine. The Citation cruised

in the free troposphere, sounding the atmosphere vertically at ~200 km intervals using "missed approaches" to airports on the way. Vertical profiles were sampled at ~600 m/min, giving a vertical resolution of ~20 m for 2 second averages. This sampling strategy, combined with interpolation to facilitate interpretation of the numerous vertical profiles, generated cross-sections showing distinct patterns due to surface fluxes at the continental scale (Fig. 3).

We observed a persistent deficit (4 - 20 ppm) of CO_2 in the lowest 2-3 km of the atmosphere during the northern survey, a clear signature of CO_2 uptake by vegetation (Fig. 3a). The smaller deficit around 84°W may indicate less uptake over the Great Lakes. However, there was a slight depletion of CO_2 in the free troposphere at the same location, which could also point to convective activity, causing mixed layer air to be vented upwards and replaced in part by free tropospheric air with higher CO_2. Enhanced CO_2 was measured during the morning take off over Massachusetts, at 71°W, due to both local emissions of fossil fuel CO_2 and night time respiration into the shallow mixed layer. Otherwise we sampled mostly the residual mixed layer from the previous afternoon in the eastern part of the transect, and the deep afternoon mixed layer in the western part, and thus we did not observe much influence from nocturnal respiration in the shallow mixed layer in the morning.

We observed enhancements of CO_2 exceeding 10 ppm in the lowest part of the atmosphere on the southern survey (Fig. 3c), in marked contrast to the northern survey. These regions of the West and Southeast were affected by strong seasonal drought, as indicated by the vegetation condition index for August 20, 2000 (Fig. 3e). This index, provided by the National Environmental Satellite, Data, and Information Service

(NESDIS) [http://orbit-net.nesdis.noaa.gov/crad/sat/surf/vci/uscd/usacd.html] and based on AVHRR radiance data, provides a measure of vegetation stress [*Kogan*, 1997]. During the southern survey, conditions were also cloudy in much of the region just upwind of the flights, further limiting photosynthesis. The unfavorable growing conditions, cloudiness, and emissions of CO_2 from fossil fuel combustion, led to enhancements of CO_2 across the whole southerly part. Over Maine, at the end of the transect, CO_2 was depleted by about 10 ppm in the lowest 2 km, but also by the same amount in the free troposphere at around 6 km. This was a clear signature of convective activity that vertically redistributed low CO_2 from the mixed layer into the middle troposphere.

The distribution of CO (Fig. 3b, 3d) exhibits notable layering with enhanced mixing ratios in the middle troposphere, caused by emissions from extensive fires in Idaho and Colorado. Mixing ratios of CO exceeding 300 ppb were found both in free tropospheric haze layers along the survey flights, and in the mixed layer of the westernmost profile of the southern survey, close to the sources. The enhanced CO in the mid troposphere coincides with aerosol layers observed by the TOMS satellite. CO from anthropogenic emissions was seen during take-off and landing near Boston, 71°W, and Denver, 105°W.

2.2. Statistical analysis

Interpretation of measurements in the lower atmosphere require an appropriate modeling framework linking local tracer mixing ratios to tracer fluxes upstream. The required resolution of a transport model is determined by the scales over which atmospheric mixing ratios vary spatially. COBRA observations provide a unique opportunity to examine these statistical properties. The distinct CO_2 signals caused by surface fluxes are mainly confined to the lower troposphere, in particular to the mixed

layer and the residual layer. Large-scale transport models cannot represent the filaments that we observed within the mixed layer, which are caused by turbulent eddies (air entrained from the free troposphere and plumes caused by rising thermals from the surface). Hence the mean value of tracer concentration averaged over the mixed layer should be the quantity compared between models and observations.

In the following sections, we analyze the accuracy of mixed layer averages determined from in situ profiles (*measurement uncertainty*), and also examine the additional uncertainty introduced when mixed layer averages are represented in transport models with finite grids (*representativeness error*). The measurement uncertainty includes limitations in instrument precision and accuracy, as well as the uncertainty of the mixed layer averages caused by atmospheric variability of CO_2 within the mixed layer due to turbulent eddies (see Fig. 4, left), which remain unresolved in transport models. The representativeness error results from the spatial mismatch between a point measurement and a model grid-cell; it is related to the "grain-size" of the spatial distribution of CO_2.

2.2.1. Uncertainty of mixed layer averages from individual profiles. To calculate mix-layer averaged mixing ratios, the mixed layer height z_i was first determined from observed tracer profiles as the altitude at which the vertical gradient of potential temperature, $d\theta/dz$, increases, as well as where step changes in H_2O, CO_2 and CO are found. The mixed-layer average CO_2 concentration ($\overline{CO_2}$) was then calculated for the over 100 profiles collected during COBRA as the mass weighted average, excluding the top 20% of the mixed layer to avoid the most active entrainment zone as well as ambiguities as to the top of the mixing zone. The standard deviation of individual

measurements in the mixed layer (Fig. 4, right) was derived by calculating the standard deviation about the mean for the whole profile in a given altitude bin over all profiles. The mean standard deviation for the 100 profiles was ~0.6 ppm for the afternoon (>14:00 local time) and ~1 ppm for morning profiles (<14:00 local time). Atmospheric variability within the mixed layer was much larger than the precision of the CO_2 instrument (1-σ ~0.13 ppm).

The variance of $\overline{CO_2}$ cannot be calculated by simply dividing the square of the standard deviation by the number of observations, since observations are spatially correlated due to the presence of tracer layers (Fig. 4, left). Instead, we can use the following approach (after [*Wei*, 1989], pg. 18) to calculate the variance of $\overline{CO_2}$; errors in $\overline{CO_2}$ are related to the square root of this variance:

$$\begin{aligned}\sigma^2\left(\overline{CO_2}\right) &= Var\left(\overline{CO_2}\right) = Var\left(\frac{1}{n}\sum_{j=1}^{n} CO_2\left(z_j\right)\right) \\ &= \frac{1}{n^2}\sum_{j=1}^{n}\sum_{k=1}^{n} Cov\left(CO_2\left(z_j\right), CO_2\left(z_k\right)\right) \\ &= \frac{1}{n}\sum_{l=-(n-1)}^{n-1}\left(1-\frac{|l|}{n}\right)\cdot\mu_l \text{ with } l = j-k\end{aligned} \tag{1}$$

Here the profiles were regridded into altitude bins (j,k) of 20m vertical, *Var* and *Cov* stand for variance and covariance, respectively, and μ_l denotes the autocovariance function at lag *l*. For simplicity the mass weighting used to calculate $\overline{CO_2}$ was neglected

in assessing errors. The error of $\overline{CO_2}$ calculated this way includes both the uncertainty introduced by the atmospheric variability and the uncertainty due to instrument precision (reproducibility within a vertical profile). Values for $\sigma\left(\overline{CO_2}\right)$ range from 0.02 to 0.9 ppm for individual profiles, with a mean over all profiles of 0.19 ppm (0.13 ppm for afternoon profiles only, and 0.22 ppm for morning profiles only). This uncertainty is an atmospheric limit imposed by unresolved turbulence when using data from the planetary boundary layer in a modeling framework. High quality instruments with errors < 0.19 ppm (1-σ) are therefore required to resolve spatio-temporal gradients in mixed-layer averages; otherwise the signal would be limited by instrument errors rather than by unresolved turbulence.

2.2.2. Spatial correlation of mixed layer averages. The geostatistical method of variogram estimation was employed to assess the spatial variability of the mixed layer averaged CO_2 (in the following referred to as signal *S*), and to derive measurement-based estimates for the representativeness error for a given spatial resolution in a transport model. The variogram is the variance of the difference of signals ($\mathrm{var}(S_i\text{-}S_j)$) measured at different locations $\mathbf{x}_i$, $\mathbf{x}_j$, as a function of distance $|\mathbf{x}_i\text{-}\ \mathbf{x}_j|$ between the points of measurement [*Cressie*, 1993]. In order to minimize the temporal variation in S, and isolate the spatial variation, we used only pairs of observations that were obtained within three hours of each other. The estimated variogram is then used to simulate many of possible realizations of the spatial distribution for *S*, consistent with a particular point measurement, allowing us to estimate the uncertainty in comparing the grid average computed by a transport model with local point measurements, i.e. the representativeness error. Details of the statistical treatment are presented in Appendix A.

Since the statistical analysis included the variance due to the measurement uncertainty, the calculated uncertainty includes both the representativeness error and the measurement uncertainty in COBRA-2000. In the following we refer to this combined error therefore as the total representativeness error, which is a measure of the uncertainty associated with using a mixed layer averaged CO_2 from a local profile measurement to represent a larger region. The results presented in Fig. 5 show a significant increase of the total representativeness error with horizontal grid size. The analysis also provided an estimate of the uncertainty in the calculated error, expressed in the range for the central 90% (indicated by the vertical bars in Figure 5). The effect of the measurement uncertainty can be seen at very small grid sizes, where the representativeness error is negligible: the total representativeness error approaches 0.2 ppm at zero grid size, consistent with the measurement uncertainty. The total representativeness error increases rapidly with grid size: at ~30 km it is twice as large as the measurement uncertainty, i.e. the representativeness error starts dominating the measurement uncertainty, and at 100 km it has increased to 0.8 ppm. These representativeness errors apply for the COBRA flights; the estimate might be different at other locations or times.

Atmospheric transport models used for inversions typically have horizontal resolution between 200 and 400 km [*Denning et al.*, 1999]; corresponding representativeness errors are 1.2 ppm to 2 ppm. This error would accrue even for a model with appropriate temporal resolution using data without the current practice of filtering out “high-frequency variability” (= signal). The COBRA data suggest that only for a grid size of ~30 km would the analysis be limited by measurement uncertainty rather than by

representativeness error. Models with coarser resolution cannot distinguish the signal contained in observed spatial variations from noise arising from representativeness error.

The variance associated with representativeness error is not random. As we show later, it is caused by the subgrid variations in surface fluxes affecting a profile. If surface fluxes in the near field environment of a measurement location are not representative for the grid scale averaged flux, biases may result.

3. Description of the Analysis Framework

An analysis framework is required that can adequately resolve the spatial variability of CO_2 as discussed in section 2, with minimal representativeness error, and extract the signal of terrestrial biospheric fluxes present in the aircraft observations (Fig. 3). Further requirements of the proposed analysis framework, outlined in Figure 1, are: (1) high temporal resolution to resolve diurnal cycles in terrestrial fluxes and boundary-layer dynamics, as well as taking into account synoptic events that introduce variations in atmospheric CO_2; (2) coupling to a boundary condition that connects tracer mixing ratios over the continent with global distributions, crucial for long-lived tracers like CO_2; (3) the ability to incorporate fossil fuel fluxes as well as fluxes from biospheric models at high temporal and spatial resolution, accounting for spatio-temporal variations in biosphere-atmosphere exchange fluxes, and providing the potential to minimize aggregation errors.

The following sections describe the different elements of the analysis framework (Fig. 1). We first introduce the receptor-oriented transport model (section 3.1) used to derive influence functions (footprints). Then the elements of the analysis framework, which are coupled to the influence functions generated by the transport model are

described, including lateral boundary conditions for CO_2 and CO mixing ratios (section 3.2), fossil fuel fluxes (3.3), and the biospheric flux model (3.4).

3.1. The receptor-oriented modeling framework

We developed a receptor-oriented modeling framework (in the following referred to as ROM) that addresses the above issues and quantitatively relates local measurements to the flux distribution upwind.

3.1.1. Theory. The ROM problem may be stated as follows: given a tracer concentration $C(\mathbf{x}_r, t_r)$ at location $\mathbf{x}_r$ measured at time t_r, what is the influence of a given surface flux upstream? We introduce the influence functions $I(\mathbf{x}_r, t_r \mid \mathbf{x}, t)$, which for a conserved tracer quantitatively link sources or sinks $S(\mathbf{x}, t)$ emitted at location $\mathbf{x}$ and at time t to the tracer amount at a receptor [*Holzer and Hall*, 2000; *Lin et al.*, 2002]:

$$C(\mathbf{x}_r, t_r) = \int_{t_0}^{t_r} dt \int_V d^3\mathrm{x}\, I(\mathbf{x}_r, t_r \mid \mathbf{x}, t) S(\mathbf{x}, t) + \int_V d^3\mathrm{x}\, I(\mathbf{x}_r, t_r \mid \mathbf{x}, t_0) C(\mathbf{x}, t_0) \tag{2}$$

The first term on the RHS represents changes in the concentration at the receptor due to surface fluxes in the domain V between initialization time t_0 and t_r. Influence I has units of inverse volume (a density); since we use mixing ratios for C (ppm), S has units of ppm/s. The second term is the contribution from advection of the initial tracer field C($\mathbf{x}$, t_0). Surface fluxes in equation 2 can be represented as interior (volume) sources or sinks

[*Holzer and Hall*, 2000], placed between surface and a column height h, chosen to be smaller than the mixed layer height z_i:

$$S(\mathbf{x},t)=\begin{cases}\dfrac{F(x,y,t)\cdot m_{air}}{h\cdot\overline{\rho}(x,y,t)} & \text{for } z\le h\\ 0 & \text{for } z>h\end{cases} \tag{3}$$

Here F is the surface flux in μmol/m^2/s, $\overline{\rho}$ is column-averaged density of air, and m_{air} is the molar mass of air. To implement surface fluxes at finite temporal (Δt) and spatial resolutions (Δx, Δy), we integrate the first term of the RHS of Eq. (2) over the discrete temporal and spatial intervals:

$$\Delta C_{i,j,k}(\mathbf{x}_r,t_r)=F(x_j,y_k,t_i)\cdot \left[\frac{m_{air}}{h\cdot\overline{\rho}(x_j,y_k,t_i)}\cdot\int_{t_i}^{t_i+\Delta t}dt\int_{x_j}^{x_j+\Delta x}dx\int_{y_k}^{y_k+\Delta y}dy\int_0^h dz\; I(\mathbf{x}_r,t_r\,|\,\mathbf{x},t)\right] \tag{4}$$

$\Delta C_{i,j,k}(\mathbf{x}_r, t_r)$ is the change in tracer amount due to fluxes $F(x_j,y_k,t_i)$ emitted from a surface grid element j, k, and in the time interval between t_i and $t_i+\Delta t$. The column-averaged density is assumed to be constant over the grid element. The term in brackets defines source-receptor elements that link surface fluxes to concentration changes at the

receptor, denoted as the "footprint element" $f(\mathbf{x}_r, t_r | x_j, y_k, t_i)$. The spatial distribution of footprint elements for a given time interval is referred to as the "footprint".

3.1.2. The STILT model. We can extract footprint information from assimilated meteorological data using the newly developed Stochastic Time-Inverted Lagrangian Transport (STILT) model [*Lin et al.*, 2002]. STILT simulates transport *backward* in time by an ensemble of trajectories for particles released at a receptor. The particles represent air parcels of equal mass, transported by mean winds and sub-grid turbulent winds calculated from surface sensible heat and momentum fluxes as represented in assimilated meteorological fields. The local particle density is directly related to the influence density. Given N_{tot} particles released from a receptor at $\mathbf{x}_r$ at time t_r, giving rise to particle density at location $\mathbf{x}$ and time t, $\rho(\mathbf{x}_r, t_r | \mathbf{x}, t)$, the influence I is given by $I(\mathbf{x}_r, t_r | \mathbf{x}, t)=\rho(\mathbf{x}_r, t_r | \mathbf{x}, t)/N_{tot}$. If we integrate I over a time interval Δt and volume element above surface grid cell (j,k), we find:

$$\int_{t_i}^{t_i+\Delta t} dt \int_{x_j}^{x_j+\Delta x} dx \int_{y_k}^{y_k+\Delta y} dy \int_0^h dz\ I(\mathbf{x}_r, t_r | \mathbf{x}, t) = \frac{1}{N_{tot}} \sum_{p=1}^{N_{tot}} \Delta t_{p,i,j,k} \tag{5}$$

The RHS is the fraction of particles found in the volume $h \cdot \Delta x \cdot \Delta y$, and $\Delta t_{p,i,k,j}$ is the time which each individual trajectory p spends in this volume above cell j,k, during the time interval Δt. STILT employs operator splitting between horizontal advection (long time step, Δt), and vertical turbulence (short time step) (details see *Lin et al.*, 2002), hence the times $\Delta t_{p,i,k,j}$ are multiples of the fast timestep. The footprint elements $f(\mathbf{x}_r, t_r | x_j, y_k, t_i)$, in Eq. 4 are therefore given by:

$$f(\mathbf{x}_r, t_r | x_j, y_k, t_i) = \frac{m_{air}}{h \cdot \overline{\rho}(x_j, y_k, t_i)} \cdot \frac{1}{N_{tot}} \sum_{p=1}^{N_{tot}} \Delta t_{p,i,j,k} \tag{6}$$

and the tracer signal due to upstream surface fluxes F ($C_{surface}$) is obtained by summing Eq. 4 over all backward timesteps (i) and surface grid elements (j,k):

$$\begin{aligned} C_{surface}(\mathbf{x}_r, t_r) &= \sum_{i,j,k} \Delta C_{i,j,k}(\mathbf{x}_r, t_r) \\ &= \sum_{i,j,k} f(\mathbf{x}_r, t_r \,|\, x_j, y_k, t_i) \cdot F(x_j, y_k, t_i) \\ &= \sum_{i,j,k} \frac{m_{air}}{h \cdot \overline{\rho}(x_j, y_k, t_i)} \cdot \frac{1}{N_{tot}} \left(\sum_{p=1}^{N_{tot}} \Delta t_{p,i,j,k} \right) \cdot F(x_j, y_k, t_i) \end{aligned} \tag{7}$$

The footprint is similar to the adjoint of a Eulerian transport model: each footprint element is equivalent to the sensitivity of the mixing ratio at a given receptor location with respect to a change in boundary (surface) flux. The approach of using a particle dispersion model to derive footprint information has multiple advantages: (1) by interpolating winds down to the exact location of a measurement, footprints can be derived at much higher spatial resolution than the driving meteorological data. This is important for the near field, close to the receptor, where influence from heterogeneous surface fluxes is strongest and footprint areas are small, allowing us to minimize *aggregation error*. (2) The representation of influence with particle distributions avoids

representativeness errors, since the volume represented by the particles at the time of the measurement is infinitesimal. However, a "sampling" error is introduced due to the finite number of particles used to represent transport to an individual measurement location. (3) Modeling turbulent transport as the ensemble of stochastically transported particles more closely approximates the stochastic nature of air parcels transported by turbulence than typical parameterizations (e.g., diffusion coefficients). (4) The fact that the model runs backward in time makes it very efficient, in that it only involves a single model run to extract the spatially and temporally resolved footprint.

For analysis of the large-scale survey data collected during COBRA, the STILT model was driven by assimilated meteorological data from EDAS (ETA Data Assimilation System) which covers the US and parts of Canada at 80 km horizontal resolution and 3 hourly updates, supplemented by GDAS (Global Data Assimilation System) data covering the northern hemisphere at ~180 km resolution with 6 hourly updates. Each run was started using EDAS winds, and meteorological grids were changed as soon as one particle left the EDAS area. Receptor points were defined along the flight track of the two large scale transects, whenever the aircraft moved vertically by about 30 mbar or horizontally by 30 km. Each receptor point released an ensemble of N_{tot} particles, with N_{tot} determined using a sensitivity test (see section 4.1). Particle positions were calculated using appropriate time steps for advection (Courant number <0.25, between 3 and 120 minutes), and for turbulence (less than 10% of the Lagrangian timescale for turbulence, 0.1 seconds to 10's of seconds). Calculations for a particle were stopped when it crossed the western model boundary (145^{o}W, see Fig. 6) or after a maximum duration of 15 days.

The particle trajectories were mapped onto a surface domain ("ROM domain") covering the continental US, Mexico and most of Canada (Fig. 6). Calculation of footprints according to Eq. (6) and coupling of transport to surface fluxes (Eq. 7) was done offline. Footprints were gridded at a maximum resolution of 1/4°lon × 1/6°lat, corresponding to roughly 20×20 km^2. To reduce computational time, the horizontal resolution of the grid at the footprint was adjusted dynamically depending on the size of the footprint area at a given timestep, keeping the number of grid elements representing the footprint between 18 and 36. All surface flux grids (section 3.3 and 3.4) were accordingly regridded before coupling to the footprints. This adjustment also prevents undersampling of surface fluxes at times when particles are spread over extensive areas with large gaps between neighboring particles.

3.1.3. Cloud venting. Cloud venting plays an important role in exchanging air between the mixed layer and the free troposphere. Unfortunately, archived meteorological fields currently lack subgrid convective fluxes from the original data assimilation model. The amount of cloud venting on unresolved scales (here 80 km) is likely to regulate a critical model property, the time τ_{exch} to replace the column of mixed layer air by air from the mid troposphere. If cloud venting is neglected, τ_{exch} is overestimated, causing an excessive build up of surface emissions in the lower atmosphere of the model.

We developed a simple parameterization of sub-grid vertical redistribution to give an upper estimate of the effect of cloud venting and provide a lower bound for τ_{exch}. We computed the limit of convection altitude, z_{LOC} (see the schematic diagram in Fig. 7), the uppermost level at which the cloud parcel is buoyant, i.e. at which its virtual temperature

is still higher than that of the surrounding air represented by the virtual temperature profile from the assimilated field. Virtual temperature in cloud was calculated by lifting a "cloud air parcel" starting at the lowest model layer, lifted dry adiabatically to the lifting condensation level (LCL), then moist adiabatically to the profile top. The presence of liquid water was neglected. We assumed that the virtual temperature from the assimilated field could be used as proxy for virtual temperature in the cloud-free environment at the levels, at which cloud and non-cloud virtual temperatures are equal (i.e. z_{LOC}).

Whenever a new update of meteorological data is read (every 3 hours for EDAS), and when z_{LOC} is higher than z_i (mixed layer height), a particle with a vertical position below z_{LOC} is assigned at each time step to a random vertical position between the surface and z_{LOC}, weighted by density. This scenario implies that cloud venting fluxes (both updrafts and downdrafts) are large enough to leave a perfectly well mixed column behind after each convective event, and that the convective events take place every 3 hours at grid cells with at least some convective available potential energy (CAPE). This simple approach represents an upper bound for the vertical redistribution caused by cloud venting, since any further vertical redistribution would not alter the particle distribution. We also conducted simulations without particle redistribution due to convection to provide a lower bound for cloud venting effects. Throughout the rest of the paper, we will present model results from these two cases, with upper-limit and zero cloud venting ("convective" and "non-convective" cases, respectively).

3.2. Lateral tracer boundary condition

The lateral tracer boundary condition is necessary to connect the regional tracer simulations to the global background tracer distribution and can be derived in principle

two ways: (*a*) a global model with sources and sinks for CO and CO_2 could be run for the period of the experiment, and the boundary condition at different times could be extracted, or (*b*) statistical procedures could be used to derive a tracer boundary field from available large scale observations. We used the second approach to derive a western boundary condition at 145 W. Because of the dominant westerly flow over the U.S., the western boundary condition represents the tracer concentrations of air parcels over the ocean before being affected by terrestrial sources and sinks. Indeed, most of the particles (about 66%) cross the 145 W after being transported for ~6 days backward from the receptor (Fig. 6), and most of the remainder (20%) reside inside the ROM domain. Only small numbers exit the domain to the north (6%), east (4%), or south (4%). The initial value (concentration of CO_2 and CO) for each particle was then calculated based on the latitude, altitude and time when it crosses the western boundary or when the calculation was stopped after 15 days. This approach neglects zonal gradients in the global tracer distribution for particles not leaving the domain to the west. However, zonal gradients are much smaller then meridional gradients; e.g. for CO_2 the difference between samples taken at Arctic stations Alert (62 W) and at Barrow (156 W) are less than 1 ppm during the month of August 2000, similarly differences between subtropical stations Kumukahi (155 W) and Bermuda (65 W) were less than 0.5 ppm, but differences the Arctic and subtropics were ~6 ppm.

Time-dependent tracer fields for CO_2 and CO (meridional cross-sections) over the Pacific were generated by statistical analysis of ground-based and airborne measurements of CO and CO_2 for the past 20 years (see Table 2). The analysis was done in two steps: first, mixing ratios at the ground were represented by an analytical function of time

derived from measurements at selected ground stations, then this function was propagated vertically to fit the airborne measurements at higher altitudes.

To retrieve continuous tracer time-series at the surface, the measurements at three selected ground stations (KUM, CBA, BRW; see Table 2) for the 20 year period starting 1/1/1980 (in case of CO_2) and for the 10 year period starting 5/26/1992 (in case of CO) were represented by its Fourier components, with a cut-off of 40 days to remove high frequency variability. CO_2 data at the CMDL stations were provided by Tom Conway [pers. com., 2001], and the GLOBALVIEW dataset [*Masarie and Tans*, 1995] was used to fill gaps in the time series before calculating the Fourier components. CO data were provided by Paul Novelli [pers. com., 2001] [*Novelli et al.*, 1998], and missing values were linearly interpolated. The CO data were corrected for an apparent drift in the CMDL standards between 1992 and 2000, causing the uncorrected data for 2000 to be low by 7 ppb (at 50 ppb) and by 2-3ppb (at 200 ppb) [Paul Novelli, pers. com., 2001]. The result of the Fourier analysis is an *analytical* representation of the time-series for CO_2 and CO, closely resembling the measurements. The standard deviation of the residuals due to the short-term variability at time scales less than 40 days was 0.9 ppm for CO_2 and 6 ppb for CO. These functions were linearly interpolated in latitude to provide surface tracer mixing ratios $CO_{2,S}(t,lat)$ and $CO_S(t,lat)$ at all required times t and latitudes lat.

To represent upper air measurements, airborne and station data collected above 300 m (see Table 2), and between the Pacific coast and 180^{o}W were merged (north of 70^{o}N the longitude range was gradually relaxed, so that at 90^{o}N all longitudes where used). We also included continental flask data collected at 8 km above Carr, Colorado, for CO_2 and CO, and CO data from Niwot Ridge, Colorado. Aircraft data with potential

influence from the stratosphere were excluded using a filter based on O_3, N_2O, CO, potential temperature, H_2O, and altitude. Flask sampling data were given a 10 fold higher weight to account for the different nature of the data compared to in-situ measurements; the 1-minute averages of the in-situ data are assumed to be not independent within a time scale of 10 minutes (assumed average duration of an atmospheric layer when sampled by an aircraft).

We used a Green's function to fit the upper air measurements for CO_2 by propagating the surface tracer mixing ratios vertically [cf. *Andrews et al.*, 1999]. The Green's function makes use of the fact that CO_2 is *conserved* in the troposphere. A simpler statistical model was fitted for CO, which is not conserved, involving an average CO gradient, an altitude dependent damping of high frequency variability, and an altitude dependent lag time. Details of the fitting procedures are given in Appendix B.

Meridional cross-sections for CO_2 and CO were generated at a resolution of 0.5 km altitude by 2.5° latitude and with a time resolution of one day, using the parameterizations derived in Appendix B (Eqs. B1 and B4). To asses the error of these fields, cross-sections were calculated on a weekly basis for the 20 year period in the case of CO_2, and for the 10 year period in case of CO, and merged with the observations. The scatter plots of calculated vs. observed tracer mixing ratios (Fig. 8) show good agreement for CO_2, with somewhat more scatter for CO in the mid and upper troposphere. Residuals in CO_2 (statistical model - measurements) have a mean of 0.26 ppm, and a standard deviation of 1.0 ppm (1 σ), only slightly larger than the 0.9 ppm standard deviation of residuals at the surface from high frequency variability (see Fig. 8). Residuals for CO

have a mean of –3.9 ppb, and a standard deviation of 21 ppb, significantly higher than the high frequency variability at the three surface stations (6 ppb).

Most of the upper atmosphere data used here were collected in campaigns, so it is possible that there is a bias due to the specific objectives of these campaigns. It is difficult, however, to assess how such a bias would affect the analysis: Large variability for CO could be caused by selective sampling of polluted layers; it is also possible that mid-tropospheric air is more influenced by proximate pollution than the marine boundary layer, thus causing higher and more variable CO. Using the mean CO_2:CO ratio from fossil fuel emissions (0.03 ppm/ppb, see section 5.2), the 21 ppb variability for CO corresponds to only 0.63 ppm of CO_2, smaller than the observed variability for CO_2.

The particle duration of 15 days is not negligible compared to an average photochemical lifetime of 30 days for CO in summer. Hence both photochemical loss due to reaction with OH and production from CH_4 oxidation were implemented in a simplified way. Climatological values for OH at the mean position (latitude and altitude) of a particle ensemble were adopted from the GEOS-CHEM OH fields [*Jaegle*, http://marzipan.atmos.washington.edu/ion_script/GEOS/main_geosoh.html], and rate constants for reactions of CO with OH and CH_4 with OH [*Atkinson et al.*, 1997] were calculated using pressure and temperature measured at the aircraft location. Oxidation of CH_4 was assumed to yield one CO per oxidized CH_4. The calculated net loss for CO was small (about 14 ppb on average, with a maximum of 30 ppb), but omitting it would give biased results. No chemical production or loss was implemented for CO from emissions (next paragraph), since most of the signal resulted from emissions close to the receptor location.

3.3. Fossil fuel fluxes

Emissions of CO_2 from fossil fuel, cement production and gas flaring were taken from the 1°×1° inventory compiled by *Marland et al.*, [1997], which is the 1995 version of the Andres et al. inventory [*Andres et al.*, 1996]. To account for changes in emissions between 1995 and 2000, a 10% increase was assumed by propagating the trend between 1992 and 1996 to 2000; due to the lower trends the years 1997 to 1999 of less than 1 % [*EPA*, 2001], this increase is likely to be high by a few percent.

Surface fluxes of CO were calculated from a combination of the NAPAP 1990 inventory for the northeastern US (1/6°Lat.×1/4°Lon.) [*EPA*, 1993] and the GEIA inventory (1°Lat.×1°Lon.) [*Benkovitz et al.*, 1996]. Since the GEIA inventory doesn't include emissions for CO, they were calculated from the low level NO_x emissions using a linear regression between NAPAP CO emissions and the GEIA low level NOx emissions in the overlapping area ($CO=12.5 \times NOx(GEIA,low)$; $R^2=0.84$). Time-of-day and day-of-week factors were applied to account for time dependence of emission fluxes [*Ebel et al.*, 1997]. Since no information on the diurnal and weekly variations are given by the CO_2 fossil fuel emission inventories, the time factors for CO emissions were also used for the CO_2 emissions; however, the amplitude of these variations was reduced by a factor of 2.5 in rough agreement with diurnal variations of anthropogenic CO_2 emissions over Japan [*Kondo et al.*, 2001].

3.4. Biosphere flux model

Terrestrial fluxes of CO_2 were modelled by linearly scaling eddy covariance observations of net ecosystem exchange (NEE) from the AmeriFlux network [*Baldocchi et al.*, 2001] for different vegetation types (denoted by *i*), projected regionally using land-cover data:

$$NEE_i = \lambda_i \cdot \left(R_i + GEE_i \right) = \lambda_i \cdot \left(\beta_i T + \frac{a_i \cdot SWRF}{b_i + SWRF} \right) \tag{8}$$

$$R_i = \beta_i T \ ; \qquad GEE_i = \frac{a_i \cdot SWRF}{b_i + SWRF} \tag{8b}$$

Here λ_i is a scaling factor (see below), R_i is the respiration flux, GEE_i is the gross ecosystem exchange, T is the atmospheric temperature in °C at 2 m; $SWRF$ is the downward short wave radiative flux from the assimilated meteorological fields (used as a proxy for photosynthetically active radiation). The parameters β_i (temperature coefficient for respiration flux, autotrophic + heterotrophic), a_i (maximum GEE), and b_i (with a_i/b_i as the quantum efficiency) were obtained from a least-square fit to the AmeriFlux data for the respective vegetation over the months July and August in 1999 (Table 3). Flux data for the year 2000 were not yet available when the analysis was done.

The IGBP 1-km resolution vegetation data [*Belward et al.*, 1999] were regridded to the ROM domain at the different horizontal resolutions starting at 1/6°Lat.×1/4°Lon., to give relative coverage for each vegetation type over the ROM domain. Since tower flux data are not available for each of the 17 different vegetation classes, the vegetation classification was simplified into 5 classes: forests, shrublands (open and closed shrublands, savannas, grassland, and barren or sparsely vegetated), croplands (croplands and cropland/natural vegetation mosaic), wetlands and water bodies. The scaling factors

λ_i then account for mismatches in the classification, up-scaling from flux-site to the larger regions, and climatic factors that may affect CO_2 fluxes in 2000. The factors λ_i, the adjustable parameters for CO_2 flux, will be estimated using the optimization described in section 5.3.

A net CO_2 flux of zero was assumed for water bodies and wetlands. The upper limit of the air-sea fluxes was estimated to be ~-0.1μmoles/m^2/s (uptake) based on recent pCO_2 data [*Lefevre et al.*, 1999]. Hence air-sea exchange fluxes are smaller than terrestrial fluxes by three orders of magnitude, and can be neglected even though a significant part of the ROM domain is covered by ocean.

4. Model tests

4.1. Dependence on particle number, reproducibility

Ideally, one would use a sufficiently large number of particles (N_{tot}) to represent the ensemble properties of the transport to a given measurement location. Since model run time increases proportionally to the number of particles used, we examined the dependence of the "sampling" error on N_{tot} in an attempt to minimize the run time. We examined the sensitivity to N_{tot} of the simulated mixed layer signal by coupling the footprints with biosphere-atmosphere exchange fluxes (i.e. we combined Eqs. 7 and 8) for five different mixed layer measurement locations along the northern survey. Particle number was varied between 50 and 1000 for each measurement location, and the model was run 100 times for each location and value for N_{tot} to derive the statistical variance (i.e. the "sampling" error). The standard deviation obeyed Poisson statistics, with stdev(CO_2)/CO_2 ~ sqrt(N_{tot}), as expected. For 100 particles the sampling error due to the stochastic nature of the model was 13%, i.e. for the 10 ppm signal observed as a deficit in

the lower atmosphere of the northern survey (Fig. 3), the statistical error was 1.3 ppm. For an average of 800 particles started within the mixed layer of each vertical sounding (N_{tot}=100 at each of 8 receptor locations), mixed layer averaged signals are reproducible within 5%, which we regard as sufficient for our purposes. The resulting computational cost was acceptable (3 minutes per receptor location for a 15-day simulation without convection for a 600 MHz processor running Linux, and twice the time with convection).

4.2. Depth of "Surface layer"

The dependence of model results (vegetation CO_2 signals) on the initial column height h (see Eq. 3) used to dilute surface fluxes at each time step was investigated by varying h between $0.1 \cdot z_i$ and $1.0 \cdot z_i$. No significant change in the modeled vegetation signal was found. However, at shallow initial column depths, the number of particles influenced by surface fluxes during a time step is smaller, which causes the statistical noise to increase. We chose a depth of $0.5 \cdot z_i$ a column height for which timescales for vertical mixing roughly matches the model timestep for advection.

5. Results

The analysis framework described in section 3 will now be used to derive regional flux estimates (Fig. 1). We first present the footprints, i.e. sensitivities of mixing ratios measured along the flight track to upstream surface fluxes (section 5.1). Then we combine measured CO_2 with advected background mixing ratios for CO_2 and an estimate of the fossil fuel contribution to CO_2 to isolate the CO_2 vegetation signal from the observations (section 5.2). In section 5.3 we use CO_2 signals due to biosphere fluxes according to Eq. 8 as constraints to optimize scaling factors (λ_i) that are consistent with

the observation based CO_2 vegetation signal, and calculate regional flux distributions and their response to meteorological conditions.

5.1. Footprints for mixed layer receptors

To visualize the surface influence and its spatial variation, we calculated time integrals of footprints over the 2 days prior to the measurement time, when surface influence is strongest. We chose receptor locations along the flight track of both surveys, at altitudes below mixed layer top (z_i). The *time integrated footprint* (Fig. 9) shows the signal in ppm found at the receptor, caused by a flux of 1 μmol m^{-2} s^{-1} from each surface location. Footprints vary on small spatial scales, especially close to the receptor. Further from the receptors, the dynamic grid resolution increased the grid size to about 1 degree. The footprints reveal a strong contrast between the northern and the southern survey, with north-westerly influence for the north, and south-westerly influence for the south. By comparing the time integrated footprints in Fig. 9 with the vegetation condition index (Fig. 3e), it becomes clear that the mixed layer in the northern survey was influenced by vegetation with fair to favorable growing conditions, while the southern survey mixed layer air, at least in the western part, was influenced by stressed vegetation. This partly explains the large differences in the observed CO_2, with a significant draw down in the lower atmosphere along the northern transect, and CO_2 emission in the southern transect (Fig. 3 a,c).

The time evolution of surface influence is shown by integrating footprints over the surface of the entire model domain, averaged over time periods ranging from 12 hours for the first 3 days back, to 72 hours for 9 to 5 days back (Figure 10). The values shown

represent signals resulting from a flux of 1 μmol m^{-2} s^{-1} acting over 24 h. They start at values around 1.5 ppm per μmol m^{-2} s^{-1}, and decay by factors of 2-3 over 48 hours. Since these *spatially integrated footprints*, they are not affected by horizontal dispersion, but only by vertical exchange processes like subsidence and cloud venting, i.e. processes which exchange air between the mixed layer (ML) and the free troposphere (FT). For transit-times which are small compared to the timescale for exchange between ML and FT (τ_{exch}) one can simply calculate spatially integrated footprints by dividing the number of molecules emitted from the surface flux (here 1 μmol m^{-2} s^{-1}) during a day by the number of molecules in the column in contact with the surface, with a height corresponding to the maximum daily z_i (mixed layer height). This gives an influence of 1.4 ppm/μmol m^{-2} s^{-1} for a z_i of 1.5 km, in agreement with the values for 0-12 hours prior to arrival in Figure 10. For transit times much longer than τ_{exch} one can assume a vertically well-mixed troposphere, for which spatially integrated footprints asymptotically approach a lower limit of 0.3 ppm/μmol m^{-2} s^{-1}. But due to the limited model domain, particles start leaving the domain, causing the spatially integrated footprints derived from particle distributions to decrease below this limit.

Figure 10 clearly shows that convection has a major impact on the decay of spatially integrated footprints with time: for the runs with convection, the influence decays to less than 1/e of the initial influence after a day, while without convection the influence needs ~5 days to decay to 1/e. These 1/e-times correspond to the timescale for mixing between mixed layer and free troposphere.

5.2. Observation-based CO_2 combustion and vegetation signals

Constraining regional/continental scale exchanges of carbon between the biosphere and the atmosphere requires isolating the biospheric signal ($\Delta CO_{2,veg}$) from the other influences on the observed CO_2 ($CO_{2,meas}$)—i.e., combustion signal ($\Delta CO_{2,comb}$) and advected background contributions ($CO_{2,bg}$; second term on the RHS of Eq. 2):

$$\Delta CO_{2,veg} = CO_{2,meas} - \Delta CO_{2,comb} - CO_{2,bg} \tag{9}$$

The advected background mixing ratio is given directly by values calculated in ROM. The combustion signal $\Delta CO_{2,comb}$ consists of emissions from fossil fuel and biomass burning:

$$\Delta CO_{2,comb} = \Delta CO_{2,ff} + \Delta CO_{2,bb} \tag{10}$$

Due to the large fires in the domain, we took an empirical approach to determining $\Delta CO_{2,comb}$, using the observed tracers instead of directly using CO_2 fossil fuel inventories. The excess of measured CO over background is an excellent tracer for biomass burning as well as for anthropogenic emissions [*Potosnak et al.*, 1999]. The enhancements in CO are then multiplied with CO_2:CO emission ratios from either fossil fuel emission inventories or from measurements in biomass burning plumes.

$$\begin{aligned} \Delta CO_{2,comb} &= \Delta CO_{2,ff} + \Delta CO_{2,bb} \\ &= \Delta CO_{ff} \cdot \left(\frac{CO_{2,ff,inv}}{CO_{ff,inv}} \right) + \Delta CO_{bb} \cdot \left(\frac{CO_2}{CO} \right)_{bb} \end{aligned} \tag{11}$$

The excess CO is due solely to combustion-derived emissions within the model domain (ΔCO_{comb}) and arises from the sum of fossil fuel emission (ΔCO_{ff}) and biomass burning (ΔCO_{bb}). ΔCO_{comb} can be derived from the observed CO and the background advected from the lateral boundary, corrected for estimated chemical production/loss:

$$\Delta CO_{comb} = \Delta CO_{ff} + \Delta CO_{bb} = CO_{meas} - \left(CO_{bg} - \Delta CO_{OH} \right) \tag{12}$$

ΔCO_{comb} (Fig. 11a, b) shows values close to zero for most of the troposphere, except for polluted layers due to anthropogenic emissions and biomass burning, where CO concentrations are elevated by more than 100 ppb. Differences between the runs without convection (Fig. 11a) and with convection (Fig. 11b) are small, indicating that the advected background CO is similar for both cases. When comparing these "measured" combustion signals to CO signals from the transport model and the inventory ($\Delta CO_{ff,inv}$, Fig. 11c, d), it is obvious that they differ significantly from each other, not only due to the lack of biomass burning emissions in the model, but also due to inappropriate convective mixing (compare to Fig. 3b). Without sub-grid convection (Fig. 11c) the model overestimates fossil fuel CO near Boston by a factor of 2, while the simulation incorporating sub-grid convection (Fig. 11d) exhibited closer agreement to measured values.

The partitioning of the contribution of biomass burning versus anthropogenic sources to ΔCO_{comb} is required to derive $\Delta CO_{2,comb}$, as the two combustion sources yield different

CO_2:CO emission ratios. Fortunately, biomass burning sources were not co-located with anthropogenic sources, and the resulting biomass burning signals were not observed at the same locations as the anthropogenic pollution (Fig. 11a, b). We identified biomass burning events, using Eq. 12, as periods when the modeled $\Delta CO_{ff,inv}$ *underestimates* the "measured" CO combustion signal ΔCO_{comb} by more than a factor of 2, and the residual was assumed to represent the biomass burning signal $\Delta CO_{bb} = \Delta CO_{comb} - \Delta CO_{ff,inv}$.

In absence of biomass burning ($\Delta CO_{bb}=0$), the CO_2 combustion signal $\Delta CO_{2,comb}$ was derived after Eq. 11, using the CO combustion signal and the inventory-based emission ratio averaged over the footprint. For very low $\Delta CO_{ff,inv}$ (<1 ppb) an average emission ratio of 0.03 ppm/ppb was assumed to avoid instability in the emission ratio $\Delta CO_{2,ff,inv}$:$\Delta CO_{ff,inv}$, and negative values for ΔCO_{comb} were set to zero to avoid "negative" fossil fuel contributions. In the presence of CO from biomass burning, fossil fuel emissions for CO_2 were adopted from the inventory-based $\Delta CO_{2,ff,inv}$, and biomass burning CO_2 was calculated as $\Delta CO_{2,bb} = (CO_2/CO)_{bb} \cdot \Delta CO_{bb}$, with the biomass burning emission ratio $(CO_2/CO)_{bb}$ estimated to be 0.0071ppm/ppb from our observed correlations in biomass burning layers.

Cross-sections of $\Delta CO_{2,comb}$ (combustion signal including biomass burning) for the northern survey are presented in Figures 11 e and f, for the cases with and without convection. They look similar, with relative differences much smaller than for inventory-based fossil fuel CO signals ($\Delta CO_{ff,inv}$, Figures 11 c and d) or for inventory-based CO_2 fossil fuel signals ($\Delta CO_{2,ff,inv}$, not shown). Thus by using the measured CO enhancements and inventory-based emission ratio, we avoid biases in combustion-related CO_2 due to inaccuracies in transport (e.g. sub-grid convection). The $\Delta CO_{2,comb}$ is influenced

predominantly by emissions from the major cities of Boston and Denver with values of up to 6 ppm, while biomass burning contributed up to 2 ppm CO_2 in the free troposphere. Uncertainties for $\Delta CO_{2,comb}$ are estimated by propagating errors in the separate terms of Eqs. 11 and 12: Uncertainties in ΔCO_{comb} are on average 23 ppb, arising from uncertainties in the boundary condition (20 ppb), in the assumed OH field (10 ppb for a 50% uncertainty in OH), and in the measurements (3 ppb). Uncertainties in $\Delta CO_{2,comb}$ due to these uncertainties in ΔCO_{comb} range from 0.1 to 2 ppm, and for CO_2 fossil fuel signals larger than 5 ppm, the relative uncertainty is 25%. Since we assume uncertainties in the CO_2/CO emission ratio to be significantly smaller than 25%, the uncertainty from ΔCO_{comb} clearly dominates. Reduction of uncertainties in the CO_2 combustion signal thus needs to come from improvements in the CO boundary condition and the parameterization for OH.

Figures 12 a and b show the signal due to biosphere-atmosphere exchange ($\Delta CO_{2,veg}$) can be derived from the measured CO_2 distribution, fossil fuel CO_2, and advected background using Eq. 9. The vegetation signal on average is an order of magnitude larger than the contribution from combustion. The strongest vegetation signals are found in the lower atmosphere of the northern survey, with a drawdown of 13-18 ppm in the west and 10-15 ppm in the eastern part. At the lowest altitudes over Massachusetts (71° W) a large positive signal of about 10 ppm was observed during the takeoff of the aircraft in the morning (8 am local time), caused by accumulation of respiration in a shallow mixed layer during the previous night.

Slightly negative values of $\Delta CO_{2,veg}$ are found in the free troposphere, with lowest values of -5 ppm observed in the middle part (84^{o}W) of the Northern survey. This

appears to be a continental scale signal of CO_2 uptake by vegetation, transported vertically to the middle troposphere by convection. The vegetation signal in the southern survey shows free tropospheric values close to zero, and a large buildup of CO_2 in the lowest kilometer exceeding 10 ppm over Kansas. Significant drawdown in CO_2 along the southern survey was only observed at the northeastern terminus, over Massachusetts and Maine; vegetation signals at his time were roughly –10 ppm in both the lower atmosphere and the free troposphere, indicating convective transport.

Uncertainties in $\Delta CO_{2,veg}$ for 0-2 km altitude due to uncertainties in the advected background field (~ 1 ppm, see section 3.2) and in $\Delta CO_{2,comb}$ (see above) are estimated to be ±1.2 ppm and ±1.4 ppm for the northern and southern surveys, respectively. These uncertainties are much larger than the ±0.19 ppm from the measurement uncertainty for mixed layer averaged CO_2 (see section 2.2).

5.3. Up-scaling AmeriFlux

In order to link the large scale constraints from the vegetation signal $\Delta CO_{2,veg}$ to eddy flux measurements made at specific sites, we scaled up the tower fluxes to the continent using the vegetation classification described in section 3.4, and Eqs. 7 and 8 to calculate the resulting vegetation signals at the aircraft location. Relative influences from the different vegetation classes for mixed layer measurements (Table 4) indicate that the dominant classes are forests and the North Pacific Ocean, followed by shrublands and croplands; less than 2% of the influence was from wetlands. For water bodies the upper limit for uptake of 0.1 μmol/m^2/s was used. So it is obvious that forests and croplands are the main contributors to uptake of CO_2 during this time of the year, accounting for about 90% of the signal.

The scaling factors λ_i for net exchange from different vegetation classes in Eq. 8 can be obtained using the measured vegetation signals ($\Delta CO_{2,veg}$, Fig. 12 a, b) as constraints, along with temperature and shortwave radiation from EDAS. We minimized the sum of squared residuals between modeled and measured vegetation signal $\Delta CO_{2,veg}$:

$$SSR = \sum_k \left(CO_{2,veg}(t_k) - \sum_{i=forest,crop} \lambda_i \cdot CO_{2,veg,mod,i}(t_k) \right)^2 \quad (13)$$

Here the t_k represent the times, when the measurements were made at the different receptor locations. To avoid calculating spurious scaling factors for classes that have only a small influence on the total vegetation signal, we fit only the two dominating vegetation classes, forest and cropland. Eq. 13 was minimized separately for the northern survey, the southern survey, and the north-eastern part of the southern survey (east of the dashed line in Fig. 12 b)), to be able to account for the large differences in the vegetation condition index for these three footprint areas.

Table 5 shows the scaling factors for forest and crop in the footprint areas of the three regions (northern survey, southern survey, and north-eastern part of southern survey), obtained for the cases with and without convection. Observed fluxes for forests in the northern footprint are in rough agreement with simple up-scaling of AmeriFlux sites (scaling factor close to 1), while southern forests are significantly less active, reflecting stressed vegetation. The strong overestimation of crop fluxes is expected, since a single AmeriFlux site within a crop field was assumed to be representative for fluxes of both IGBP classes “cropland” and “cropland/natural vegetation mosaic”. However, the cropland was evidently less active in the southern footprint area, with a scaling factor not

significantly different from zero, likely due to differences in harvesting cycles and seasonal drought. The fluxes calculated for the convective case are significantly stronger than the non-convective case. This is caused by dilution of surface signals to higher altitudes, resulting in a footprint that is confined to a smaller area, and to a shorter time-span, for the convective case (see Fig. 10).

NEE for the whole surface domain was calculated on a 3-hourly time step for the month of August 2000 using Eq. 8, with surface temperature and downward shortwave radiative flux from the EDAS fields, and the scaling factors from the non-convective case. The resulting estimates for the 24-hour averaged net biosphere-atmosphere fluxes for the non-convective case are shown in Figure 13. Diurnally averaged fluxes range from 4 μmole/m^2/s uptake to 1 μmole/m^2/s release of CO_2. Most striking is the variability of fluxes, both in space and time: in the footprint area of the northern survey (Fig. 13, top) patches of low uptake are located next to areas with strong uptake, and these areas change from day to day. This variability is dominated by moving cloud systems: A band of clouds covered the Great Lakes and areas north on the 17th, and moved to the east on the following days, reducing photosynthetic uptake. In the footprint area of the southern survey simulated fluxes are small, with less temporal variability. Spatial variability was associated with vegetation patterns in the western end of the flight area.

6. Discussion

COBRA can be viewed as a snapshot of data that could be provided by future sampling networks with enhanced spatial coverage and multiple profiles. We developed a receptor-oriented analysis to specify the footprint areas where surface fluxes influence mixing ratio measurements in the mixed layer. Footprints are typically limited to an area

of about 10^5 km^2 (Fig. 9) and to the few days preceding the measurement (Fig. 10) at individual receptor locations. A dense network of stations with long-term accurate mixing ratio measurements (e.g., instrumented tall towers) will provide time series of CO_2 distributions with similar spatial variability as observed during COBRA, at least during the growing season. The footprint area for a given measurement station will change, depending on meteorological conditions, thereby covering a larger area when aggregating over time.

A diagnostic model to infer regional and continental scale fluxes on seasonal, annual and longer time scales from atmospheric measurements should account for the processes that cause atmospheric variability. One cannot assume that it is appropriate to average over unresolved spatial and temporal variability, because significant biases may be introduced: For example, coarse vertical resolution and inappropriate representation of boundary layer mixing may cause biases due to the rectifier effect [*Denning et al.*, 1996]. A similar situation can arise when cloud venting is not appropriately represented: if occurrence of cloud venting covaries with CO_2 fluxes, as would be expected due to the dependence of both on solar radiation, biases in the flux estimate are likely. Biases can also result when systematic patterns in wind direction, diurnally or synoptically, are not properly resolved, due to anisotropy of CO_2 fluxes in the near field surrounding a measurement station.

The receptor-oriented approach attempts to represent the processes that could potentially introduce biases in flux estimates, with a stochastic simulation of mixed layer turbulence, a simplified cloud-venting scheme, and with a coupling between transport and surface fluxes at high resolution to resolve the near field of the measurement

locations. This framework is analogous to a regional adjoint model in a Eulerian framework; both require boundary conditions from either a global model or from a climatology based on measurements. One difference is that the receptor-oriented approach resolves variations in surface flux on scales smaller than the grid of the meteorological fields.

To assess how successfully the approach resolves the spatial and temporal variability in CO_2 mixing ratios, we compare simulated CO_2 vegetation signals $\Delta CO_{2,veg,mod}$ with "measured" vegetation signals $\Delta CO_{2,veg}$ derived in section 5.2. The simulated distribution of CO_2 vegetation signals $CO_{2,veg,mod}$ for the different surveys and the different model cases are shown in Figs. 14 a-d. In general there is reasonable agreement between the modeled (Fig. 14) and the "measured" (Fig. 12) cross-sections. Both exhibit the strong depletion of CO_2 in the lower atmosphere for the northern survey, and a build up of CO_2 in the middle of the southern survey. Correlation coefficients between $CO_{2,veg,mod}$ and $CO_{2,veg}$ reach values of r^2=0.5 for the northern survey in the non-convective case. However, there are numerous discrepancies, which in general can be related to: (1) inadequate representation of atmospheric transport; (2) oversimplified representation of biosphere; and (3) uncertainties in the measured CO_2 vegetation signal. In the following paragraphs we discuss errors in modeled vegetation signals due to (1) and (2), and their effect on the simulated large-scale distribution of vegetation CO_2; (3) has been discussed in section 5.2.

6.1. Discrepancies related to transport representation

Transport errors can arise from inadequate parameterizations within STILT (e.g., convection, mixed layer height, turbulence statistics) and from errors in the assimilated

winds used to drive STILT, either due to the assimilation process itself, or by inadequate post-processing [*Lin et al.*, 2002].

The clearest discrepancies are caused by the extremes in vertical redistribution built into the convective parameterization: In the westernmost profile of the northern transect the model case with convection (Fig. 14 c) overestimates the vertical dilution of $\Delta CO_{2,veg,mod}$, while the non-convective case (Fig. 14 a) shows reasonable agreement with the observations (Fig. 12 a). For the easternmost profile of the southern transect it is the opposite: no vegetation signal was found around 6 km in the non-convective case, while a significant depletion of CO_2 resulted from the convective case (see Figs. 12 b, 14 b and 14 d). In this example convection was active in the footprint area during the afternoon on the day before the flight. This indicates that the two cases (excessive convection and no convection) bound the true influence of convection on the tracer distribution. However, the strong impact of convection on the derived fluxes (see scaling factors, Table 5) indicates the necessity for a convection scheme to accurately quantify cloud venting, with realistic temporal variations to avoid biases in simulated CO_2 due to covariation with surface fluxes. Clearly assimilated meteorological products should include convective fluxes, and the convective parameterizations in the assimilation model needs to be realistic.

In the middle of the northern survey, at 83 W, the nearly flat profile of $\Delta CO_{2,veg}$ with a depletion in the lowest 2 km of only 2-3 ppm, and free tropospheric vegetation signals of -1.2 ppm, is not reproduced by either model case. Both give –9 ppm in the lower altitudes, similar to other portions of the survey. A potential explanation for this discrepancy can be seen from Fig. 13: surface fluxes are strongly influenced by a cloud

system moving from the Great Lakes region towards the north-east, and the amount of CO_2-depletion in the sampled air depends critically on the relative location of footprint area and the cloud system at a given time. Reduced cloud cover (or higher incident radiation) over the footprint area in the simulation can cause substantial changes in CO_2 vegetation signals. A further contribution to this discrepancy might be unresolved mesoscale circulations in the proximity of the Great Lakes, yielding wrong estimates for the footprint close to the receptors, where influence is strongest (see Fig. 9). Significant errors can accrue if the assimilation model misrepresents clouds in the footprint, as might be expected around the Great Lakes, or in areas near frontal systems.

Throughout the profiles of both surveys there is a significant underestimation of the nighttime build-up of respiration signal in the early morning mixed layer, and an overestimation at levels in the residual layer. The problem results from slightly too much vertical mixing: residual layer receptors at altitudes of around 500 m agl are influenced by the surface during night time in the dispersion model, whereas the strong vertical gradients of tracer indicate a clear mixing barrier at low levels in the atmosphere. The ability to use the information contained in the nighttime buildup of respired CO_2 is crucial to independently constrain fluxes due to nighttime release and daytime uptake of CO_2. The difficulty in partitioning respiration and uptake of CO_2 can be illustrated, when solving for independent scaling factors for respiration and assimilation using Eqs. 8 and 13: these scaling factors exhibit significant correlation ($r>0.97$). This suggests that the nighttime release and daytime uptake cannot be independently estimated. An improvement can only be expected from more sophisticated mixing schemes in models during night time.

As discussed by *Lin et al.* [2002], lack of mass conservation in EDAS winds leads to inaccuracies in source-receptor relationships. These inconsistencies are related to the post-processing of wind fields (degradation of resolution and non-mass conserving transformations in the vertical coordinate and horizontal re-projections), and to the assimilation process in the weather prediction model itself. Violations of mass conservation are likely to have an impact on the retrieved vegetation CO_2 signals, but the magnitude of the error is difficult to estimate. Using mass conserving wind fields, or correcting wind fields to conserve mass has therefore a high priority.

6.2. Discrepancies related to representation of the biosphere

The assumption made in the simple parameterization of biosphere-atmosphere flux is that a given vegetation class within the footprint area for a given survey (north or south) has a light and temperature response similar to the AmeriFlux data from July and August 1999 representing this vegetation class. The use of prior year data could cause some difficulties, since there are significant differences in the vegetation condition index between 1999 and 2000 (Fig. 3 e and 3 f). The assumption of spatial homogeneity within a vegetation class over the footprint areas re-introduces an aggregation error, problematic given significant spatial differences in vegetation health, and the broad range of vegetation types included in one of our coarse classes, within a footprint (Fig. 3 e and Fig. 9). There are two approaches to reduce this source of aggregation error: one can decrease the size of the flux region, and thus solve for more parameters which can adjust the spatial flux pattern, or one can improve the spatial distribution of fluxes, e.g. by adding information on vegetation health, or by using a full biosphere model which

describes phenomena such as drought stress. The former approach of course would limit the ability to predict errors, since the degrees of freedom are reduced.

Future work will include the implementation of a more sophisticated representation of the biosphere, e.g. using information on leaf nitrogen, on crop data from USDA (e.g., harvesting cycles), and perhaps the use of satellite-derived quantities such as the vegetation condition index and NDVI. The important capability of this receptor-oriented framework, however, is that it can be coupled to any surface flux patterns at high spatial and temporal resolution, such as can be generated by a full biospheric model. Ultimately one would not optimize for fluxes on some regional scale, but for parameters controlling uptake and respiration in a spatially-explicit biosphere model.

To assess the spatial variability in CO_2 mixing ratios associated with fine-scale variance of the surface fluxes, we ran the receptor-oriented model with 16-fold degradation in spatial resolution (from 20 to 80 km). Differences in simulated CO_2 for mixed layer receptors on the northern survey were 0.5 ppm (standard deviation), nearly matching the dependence on resolution of the representativeness error (Fig. 5).

The uncertainties arising from inappropriate representation of atmospheric transport and biospheric fluxes will need to be addressed in the future to ensure the success of a continental monitoring network in inferring regional and continental fluxes. The same issues apply in both Lagrangian and Eulerian models.

7. Concluding remarks

We have analyzed COBRA data to test critically the requirements of a model-data fusion system aimed at deriving regional to continental flux estimates from measurements of CO_2 over the continent. The spatial patterns in the CO_2 data collected

over the U.S. during COBRA show clear signatures of terrestrial fluxes during the active growing season. Accurate instruments enable measurement of mixed-layer averages from vertical profiles with an uncertainty of 0.2 ppm (limited solely by unresolved turbulence), providing tight constraints for fluxes when used in an appropriate modeling framework. A significant fraction of the information in these signatures, however, is contained in relatively small spatial and temporal scales. In order to effectively use the information contained in accurate CO_2 measurements, transport models need to resolve these scales; otherwise this fine-scale signal is transformed into large-amplitude unresolved variance. The high horizontal variability of the mixed layer averaged CO_2 indicates that the representativeness error (mismatch between local observation and grid average model value) dominates over the measurement uncertainty at a horizontal resolution of 30 km or larger.

The receptor-oriented framework that we developed extracted the signal of terrestrial flux causing variability in continental CO_2 observations. It consisted of (1) a Lagrangian transport model (STILT) to extract the adjoint solution from assimilated winds, (2) lateral boundary conditions for CO_2 and CO from a climatological analysis, and (3) surface boundary conditions for fossil fuel and biospheric fluxes. This framework allowed us to calculate vegetation signals $\Delta CO_{2,veg}$ along the COBRA flight track as the difference between measured CO_2 and the sum of advected boundary mixing ratios and combustion signal. Simultaneous observations of CO enabled improved estimates of the combustion signal $\Delta CO_{2,comb}$. The vegetation signals provided a tight constraint for large-scale biosphere-atmosphere exchange fluxes from up-scaling of AmeriFlux measurements.

Modeled vegetation signals explained up to 50% of the observed variance, reasonable agreement in light of the shortcomings of the transport fields currently available.

Discrepancies between modeled vegetation signals and vegetation signals derived from airborne observations revealed a variety of problems which have to be addressed in future studies: (1) an accurate convection scheme is required for a long-lived tracer with surface sources/sinks like CO_2 that is very sensitive to vertical redistribution; (2) in order to separate respiration and assimilation of CO_2, improvements in mixing schemes during nighttime periods are required; (3) offline transport models using assimilated winds can be subject to violations of mass conservation, which can have a significant effect on the accuracy of source-receptor relationships; (4) large variations in biosphere-atmosphere exchange result from the reduction of downward radiation due to cloud systems, and it is important to accurately represent these systems and their effect on radiation in the footprint area of CO_2 measurements; and (5) the overly simplified biospheric representation, assuming spatially and temporally constant light and temperature responses, is inadequate to yield accurate relationships between large-scale and local fluxes. Fluxes from a full biosphere model can and should be coupled to the receptor-oriented framework in the future, with focus on estimating biospheric parameters rather than scaling factors in the values of fluxes.

When examining these large scale measurements as a snapshot of the data that would be collected by a future sampling network (as suggested by the NACP), one would be interested in quantifying not only large fluxes during the growing season, but more importantly long-term (e.g. net annual) exchange fluxes over regional to continental scales. Thus the uncertainties have to be put in a long-term context, and it becomes very

important how the errors are correlated from day to day, i.e. whether the uncertainties accumulate to a bias on seasonal to annual timescales, or whether the uncertainties are only correlated over short timescales, so that integration over longer time periods reduces the resulting uncertainties. Future programs such as the NACP will provide data with enhanced temporal and spatial coverage, which will allow us to assess these unresolved issues.

We envision a variety of future applications for the receptor-oriented framework presented here. The framework can be applied to long-term measurements, e.g. from instrumented towers, of CO_2, CO, and other tracers like CH_4 to provide information on regional fluxes over annual and interannual timescales. The capability to calculate quantitative footprint estimates, resolving influences from different vegetation types, is invaluable to evaluate the design of hypothetical observational networks. When coupled to a full biospheric model, the framework could enable assimilation of atmospheric observations to constrain parameters controlling both short-term, rapid process and slow processes in the carbon cycle at continental and regional scales.

Appendix A

Variogram estimation and model fitting

First, a dataset of pairs was created containing S_i-S_j and $|x_i - x_j|$, where all possible combinations of two observations where used that were measured within 3 hours of each other, giving 317 different pairs. A plot of $|S_i - S_j|$ vs. $|x_i - x_j|$ is shown in Fig. A1. The data were grouped by distances into equal sized groups of 30 pairs, with the last group containing 47 pairs. For the pairs in a given group with average distance $|x_i - x_j| = h$ a variogram was estimated using a robust variogram estimator [*Cressie*, 1993]

$$Var\left(S_i - S_j\right) = 2\bar{\gamma}\left(h\right)$$
$$= \left\{ \frac{1}{N\left(h\right)} \sum_{N(h)} \left| S_i - S_j \right|^{1/2} \right\}^4 \Bigg/ \left(0.457 + \frac{0.494}{N\left(h\right)} \right) \qquad \text{(A1)}$$

Here *N(h)* is the number of pairs in the group with distance *h*; $\bar{\gamma}\left(h\right)$ is called the semi-variogram. Variogram estimates ($2\bar{\gamma}\left(h\right)$) are shown vs. distance *h* in Figure A2 as filled squares.

In order to allow a spatial simulation of the process, a variogram model has to be fit to the discrete variogram estimates from data, giving a variogram value at any given distance. There are a number of variogram models, for which the main requirement is that they have to be negative definite (in equivalence to that a covariance must be positive definite) [*Cressie*, 1993]. Out of these different variogram models (Linear, Gaussian, Exponential, Rational quadratic, and Power) the Power-variogram was chosen:

$$2\gamma\left(h\right) = 2\left(c_0 + c_1 \cdot h^{\lambda}\right) \qquad \text{(A2)}$$

Here c_0 is the nugget (variance caused by the measurement uncertainty $\sigma\left(\overline{CO_2}\right)$, taken from eq. 1), and c_1 and λ (power) are parameters to be estimated. Since the variogram estimates from Eq. A1 are not statistically independent (many distance-groups of pairs share common individual observations), a covariance matrix was estimated using a Jackknife (delete-1) statistics: The variogram estimation was repeated with one observation (mixed layer average CO_2 and position) deleted at a time (gray symbols in Figure A2), and the variogram error for each distance-group was estimated according to

the classical Jackknife statistics [*Cressie*, 1993]. The Power variogram was then fitted using a weighted generalized least square, taking the error covariance into account (solid line in Fig. A2). The power variogram fit the data reasonably well, especially in that, for small distances, it exhibits a small slope, avoiding overestimation at small distances typical of many other variogram models. At 150 km and 180 km distance, the fit doesn't go through the variogram estimates, however, this is caused by the large error for the variogram estimate at these distances, combined with smaller errors at smaller distances. Also, the Power-variogram will fail at larger distances, since the differences between mixed layer mean signals will not exceed certain values, no matter how far the locations are apart, so one would expect the true variogram to approach some limit on large scales. However, here we are interested in the regional scale, and our approach gives a conservative estimate (lower limit for the variogram).

Spatial simulation, representativeness error

The spatial simulation was done following Cressie [1993]. The simulation was conducted on regular quadratic grids with 20×20=400 elements for two different grid distances (5 km and 50 km grid size). For each distance (using a 400×400 matrix of all possible pairs of grid elements) the variogram was calculated using the fitted Power-variogram, and the covariance was estimated using the following relation:

$$\begin{aligned} Var\left(S_i - S_j\right) &= Var\left(S_i\right) + Var\left(S_j\right) - 2 \cdot Cov\left(S_i, S_j\right) \\ &= 2 \cdot Var\left(S\right) - 2 \cdot Cov\left(S_i, S_j\right) \\ \Rightarrow Cov\left(S_i, S_j\right) &= Var\left(S\right) - Var\left(S_i - S_j\right)/2 \end{aligned} \tag{A3}$$

Here the variance *Var(S)* was assumed to be independent of the location (the following simulation doesn't depend on this offset in the covariance), such that the covariance is assumed to be only a function of distance. The spatial simulation starts with a field populated by uncorrelated random numbers $\boldsymbol{\varepsilon}$, with unit variance and zero mean. The simulated spatial distribution is then calculated through $\mathbf{S}=\text{mean}(\mathbf{S})+\boldsymbol{\Sigma}^{1/2}\cdot\boldsymbol{\varepsilon}$, where $\boldsymbol{\Sigma}^{1/2}$ is the "square root" of the covariance matrix $\boldsymbol{\Sigma}$ ($\boldsymbol{\Sigma}^{1/2}=\mathbf{Q}\,\boldsymbol{\lambda}^{1/2}\,\mathbf{Q'}$, with Q the matrix whose columns are the eigenvectors of $\boldsymbol{\Sigma}$ and with $\boldsymbol{\lambda}^{1/2}$ as a diagonal matrix with the square roots of the eigenvalues). Fig. A3 shows the results of a simulation (one of the ensemble of possible realizations) for the 50 km grid. It is obvious that the variogram determines a certain grain-size for the CO_2 distribution, a size over which the concentration doesn't change more than a given tolerance value.

The representativeness error depends on the grid size of a transport model, and can be obtained from the spatial simulations (Fig. A3) for a given grid size. We calculated the representativeness error for a model with resolution of e.g. 200 km as the standard deviation of individual point values within all sub grids of size 200×200 km, averaged over 50 simulations. The calculated error (Fig. 5) includes both the representativeness error and the measurement uncertainty, since the fitted variogram model included the variance due to the measurement uncertainty. The range of possible values for the representativeness error was estimated by repeating the simulations with extreme parameter values from the variogram (5 and 95 percentiles).

Appendix B

Fitting of upstream CO_2 data over the Pacific

The data were grouped into two latitude bands (south and north of 37.5°N), and into altitude bins, with ranges 0-2.5, 2.5-5, 5-8, and above 8 km. To propagate the CO_2 time series vertically, daily averaged mixing ratios $CO_{2,z}(t,lat)$ measured within altitude bin j and at latitude bin i were related to the time-series at the surface $CO_{2,S}(t',lat)$ by the Green's-function $G_{i,j}(t-t')$ for the 1-D advection-diffusion equation, similar to the approach used by *Andrews et al.* [1999] for stratospheric CO_2:

$$CO_{2,z}\left(t,lat\right)=\int G_{i,j}(t-t')\cdot CO_{2,S}\left(t',lat\right)\cdot dt \tag{B1}$$

with:

$$G_{i,j}(t-t')=\frac{a}{\sqrt{\left(t-t'\right)^3}}\cdot\exp\left(-b_{i,j}\left(t\right)\cdot\left(t-t'\right)-\frac{c_{i,j}(t)}{t-t'}\right) \tag{B2}$$

Parameter $b_{i,j}(t)$ controls the decaying behavior at large $t-t'$, while $c_{i,j}(t)$ controls the behavior at small $t-t'$. a is an integration constant to normalize G. The timescales $1/b_{i,j}(t)$ and $c_{i,j}(t)$ are allowed to be time dependent, parameterized by a sinusoidal with a one year cycle:

$$\begin{aligned} b_{i,j}(t)&=\frac{b_{i,j}}{1+s_i\cdot\sin\left(2\pi\cdot(t-t_0)/T\right)}\\ c_{i,j}(t)&=c_{i,j}\cdot\left(1+s_i\cdot\sin\left(2\pi\cdot(t-t_0)/T\right)\right)\end{aligned} \tag{B3}$$

Here T is one year, and t_0 was empirically chosen as 1st of October to allow for smaller time scales in summer (faster vertical transport). The parameter s_i controls the amplitude of the seasonal variation of the timescales. The parameters $b_{j,i}$, $c_{j,i}$, and s_i for the 2 latitude bands and the 4 altitude bins, i.e. a total of 18 parameters, were estimated by least square optimization using a total of 11500 observations (see Table 2).

This framework of a 1-dimensional system with a boundary condition at the ground (z=0) is not very realistic (the sources for CO_2 at higher altitudes are usually not exactly underneath at the same horizontal location), but it is practical: It provides a way to relate upper air measurements of CO_2 to surface measurements with a certain time-lag (causing the seasonal cycle to occur later or earlier at higher altitudes), and with a damping of higher frequency variations via the width of $G(t\text{-}t')$ which reflects the effect of atmospheric mixing processes. Further it makes use of the fact that CO_2 is *conserved* in the troposphere.

Fitting of CO data

To propagate the CO time series vertically, a different approach had to be used, since CO (unlike CO_2) is *not conserved* in the troposphere. The data were grouped into three different latitude bands (10-37.5°N, 37.5-62.5°N, 62.5-70°N); these bands are centered over the surface stations. The CO time series at the surface $CO_S(t,lat)$ was separated into a slow component $CO_{slow}(t,lat_i)$ (timescales longer than 1 year) and a fast component $CO_{fast}(t,lat)$ (timescales 1 year to 40 days). The following parameterization was chosen to fit measured mixing ratios $CO_z(t,lat)$ at higher altitudes:

$$\begin{aligned} CO(t,z,lat) = {} & CO_{slow}(t - f_i \cdot z, lat) + d_i \cdot z \\ & + (1 + e_i \cdot z) \cdot CO_{fast}(t - f_i \cdot z, lat) \end{aligned} \tag{B4}$$

Here, parameter d_i represents an average vertical CO gradient for latitude bin i, which is required to account for photochemical losses of CO, e_i reflects the damping of the seasonal cycle (and higher frequencies) with increasing altitude, and f_i is the change of the lag time with altitude. These 3 parameters were estimated by using a least square fit at each latitude bin from a total of 12498 observations.

Acknowledgments. We acknowledge Roland R. Draxler for providing the Hybrid Single-Particle Lagrangian Integrated Trajectory (HYSPLIT) source code. For CO and CO_2 data from the Cooperative Air Sampling Network we acknowledge the National Oceanic and Atmospheric Administration (NOAA), Climate Monitoring and Diagnostics Laboratory (CMDL), Carbon Cycle Group. We thank Stephanie Vay (NASA) and Glen Sachse (NASA) for their CO_2 data collected aboard the NASA DC-8, and Andre Prevot, Richard Schillawski and Greg Kok for providing the ACE-1 CO_2 data. CO and CO_2 data from many airborne missions were obtained from the NASA Langley Research Center Atmospheric Sciences Data Center, and from NASA Ames Research Center Earth Science Projects Office Missions. COBRA was funded by NSF [ATM-9821044], DOE [DE-FG02-98ER62695], NASA [NAG5-7950], and NOAA [NA06GP0406].

References

Andres, R.J., G. Marland, I. Fung, and E. Matthews, A one degree by one degree distribution of carbon dioxide emissions from fossil-fuel consumption and cement manufacture, 1950-1990, *Global Biogeochemical Cycles*, *10* (3), 419-429, 1996.

Andrews, A.E., K.A. Boering, B.C. Daube, S.C. Wofsy, E.J. Hintsa, E.M. Weinstock, and T.P. Bui, Empirical age spectra for the lower tropical stratosphere from in situ observations of CO_2: implications for stratospheric transport, *Journal of Geophysical Research*, *104* (D21), 26581-26595, 1999.

Atkinson, R., D.L. Baulch, R.A. Cox, F.R.J. Hampson, J.A. Kerr, M.J. Rossi, and J. Troe, Evaluated kinetic and photochemical data for atmospheric chemistry: Supplement V, *J. Phys. Chem. Ref. Data*, *in press*, 1997.

Bakwin, P.S., P.P. Tans, C. Zhao, W.I. Ussler, and E. Quesnell, Measurements of carbon dioxide on a very tall tower, *Tellus*, *47B*, 535-549, 1995.

Bakwin, P.S., P.P. Tans, D.F. Hurst, and C. Zhao, Measurements of carbon dioxide on very tall towers: results of the NOAA/CMDL program, *Tellus*, *50B*, 401-415, 1998.

Baldocchi, D., and e. al., FLUXNET: A new tool to study the temporal and spatial variability of ecosystem-scale carbon dioxide, water vapor and energy flux densities, *BULLETIN OF THE AMERICAN METEOROLOGICAL SOCIETY*, *82* (11), 2415-2434, 2001.

Belward, A.S., J.E. Estes, and K.D. Kline, The IGBP-DIS global 1-km land-cover data set DISCover: a project overview, *Photogrammetric Engineering & Remote Sensing*, *65* (9), 1013-1020, 1999.

Benkovitz, C.M., M.T. Scholtz, J. Pacyna, L. Tarrason, J. Dignon, E.C. Voldner, P.A. Spiro, J.A. Logan, and T.E. Graedel, Global gridded inventories of anthropogenic emissions of sulfur and nitrogen, *Journal of Geophysical Research-Atmospheres*, *101* (D22), 29239-29253, 1996.

Bousquet, P., P. Ciais, P. Peylin, M. Ramonet, and P. Monfray, Inverse modeling of annual atmospheric CO_2 sources and sinks 1. method and control inversion, *Journal of Geophysical Research*, *104* (D21), 26161-26178, 1999.

Chou, W.W., S.C. Wofsy, R.C. Harriss, J.C. Lin, C. Gerbig, and G.W. Sachse, Net fluxes of CO_2 in Amazonia derived from aircraft observations, *Journal of Geophysical Research*, *accepted*, 2002.

Conway, T.J., P.P. Tans, L.S. Waterman, K.W. Thoning, D.R. Kitzis, K.A. Masarie, and N. Zhang, Evidence for interannual variability of the carbon cycle from the National Oceanic and Atmospheric Administration/Climate Monitoring and Diagnostics Laboratory Global Air Sampling Network, *Journal of Geophysical Research*, *99* (D11), 22831-22855, 1994.

Cressie, N.A.C., *Statistics for Spatial Data*, J. Wiley & Sons, 1993.

Daube, B.C., K.A. Boering, A.E. Andrews, and S.C. Wofsy, A high-precision fast-response airborne CO_2 analyzer for in situ sampling from the surface to the middle stratosphere, *submitted to JGR*, *accepted*, 2002.

Denmead, O.T., M.R. Raupach, F.X. Dunin, H.A. Cleugh, and R. Leuning, Boundary layer budgets for regional estimates of scalar fluxes, *Global Change Biology*, *2*, 255-264, 1996.

Denning, A.S., D.A. Randall, G.J. Collatz, and P.J. Sellers, Simulations of terrestrial carbon metabolism and atmospheric CO_2 in a general circulation model. Part 2: Simulated CO_2 concentrations, *Tellus*, *48B*, 543-567, 1996.

Denning, A.S., M. Holzer, K.R. Gurney, M. Heimann, R.M. Law, P.J. Rayner, I.Y. Fung, S.M. Fan, S. Taguchi, P. Friedlingstein, Y. Balkanski, J. Taylor, M. Maiss, and I.

Levin, Three-dimensional transport and concentration of SF6 - A model intercomparison study (TransCom 2), *Tellus Ser. B-Chem. Phys. Meteorol.*, *51* (2), 266-297, 1999.

Ebel, A., R. Friedrich, and H. Rodhe, Tropospheric Modelling and Emission Estimation, in *Transport and Chemical Transformation of Pollutants in the Troposphere*, edited by P. Borell, P.M. Borell, T. Cvitas, K. Kelly, and W. Seiler, Springer-Verlag, Berlin Heidelberg, 1997.

EPA, Regional Interim Emission Inventories (1987-1991), Volume I and II, United States Environmental Protection Agency, Research Triangle Park, N.C., 1993.

EPA, Inventory of U.S. greenhouse gas emissions and sinks: 1990 - 1999, United States Environmental Protection Agency, 2001.

Fan, S., M. Gloor, J. Mahlman, S. Pacala, J. Sarmiento, T. Takahashi, and P. Tans, A large terrestrial carbon sink in North America implied by atmospheric and oceanic carbon dioxide data and models, *Science*, *282*, 442-446, 1998.

Gerbig, C., D. Kley, A. Volz-Thomas, J. Kent, K. Dewey, and D.S. McKenna, Fast response resonance fluorescence CO measurements aboard the C-130: instrument characterization and measurements made during North Atlantic REgional Experiment 1993, *Journal of Geophysical Research*, *101* (D22), 29229-29238, 1996.

Gerbig, C., S. Schmitgen, D. Kley, A. Volz-Thomas, K. Dewey, and D. Haaks, An improved fast-response vacuum-UV resonance fluorescence CO instrument, *Journal of Geophysical Research*, *104* (D1), 1699-1704, 1999.

GLOBALVIEW-CO2, : Cooperative Atmospheric Data Integration Project - Carbon Dioxide., NOAA CMDL, Boulder, Colorado, 2001.

Gloor, M., S.-M. Fan, S. Pacala, J. Sarmiento, and M. Ramonet, A model-based evaluation of inversions of atmospheric transport, using annual mean mixing ratios, as a tool to monitor fluxes of nonreactive trace substances like CO_2 on a continental scale, *Journal of Geophysical Research*, *104* (D12), 14245-14260, 1999.

Haszpra, L., Z. Barcza, P.S. Bakwin, B.W. Berger, K.J. Davis, and T. Weidinger, Measuring system for the long-term monitoring of biosphere/atmosphere exchange of carbon dioxide, *Journal of Geophysical Research*, *106* (D3), 3057-3069, 2001.

Holloway, J.S., R.O. Jakoubek, D.D. Parrish, C. Gerbig, A. Volz-Thomas, S. Schmitgen, A. Alan Fried, B. Wert, B. Henry, and J.R. Drummond, Airborne intercomparison of vacuum ultraviolet fluorescence and tunable diode laser absorption measurements of tropospheric carbon monoxide, *J. Geophys. Res.*, *105* (D19), 24251-24261, 2000.

Holzer, M., and T.M. Hall, Transit-time and tracer-age distributions in geophysical flows, *Journal of the Atmospheric Sciences*, *57* (21), 3539-3558, 2000.

Kaminski, T., P.J. Rayner, M. Heimann, and I.G. Enting, On aggregation errors in atmospheric transport inversions, *Journal of Geophysical Research*, *106* (D5), 4703-4715, 2001.

Kogan, F. N., 1997: Global Drought Watch from Space, *Bulletin of the American Meteorological Society, 78,* 621-636.

Kondo, H., N. Saigusa, S. Murayama, S. Yamamoto, and A. Kannari, A numerical simulation of the daily variation of CO2 in the central part of Japan, *Journal of the Meteorological Society of Japan*, *79* (1), 11-21, 2001.

Kuck, L.R., T. Smith Jr., B.B. Balsley, D. Helmig, T.J. Conway, P.P. Tans, K. Davis, M.L. Jensen, J.A. Bognar, R.V. Arrieta, R. Rodriquez, and J.W. Birks, Measurements

of landscape-scale fluxes of carbon dioxide in the Peruvian Amazon by vertical profiling through the atmospheric boundary layer, *Journal of Geophysical Research*, *105* (D17), 22137-22146, 2000.

Lefevre, N., A.J. Watson, D.J. Cooper, R.F. Weiss, T. Takahashi, and S.C. Sutherland, Assessing the seasonality of the oceanic sink for CO2 in the northern hemisphere, *GLOBAL BIOGEOCHEMICAL CYCLES*, *13* (2), 273-286, 1999.

Lin, J.C., C. Gerbig, S.C. Wofsy, B.C. Daube, A.E. Andrews, P.S. Bakwin, K.J. Davis, J. Stith, and A. Grainger, A Near-Field Tool for Simulating the Upstream Influence of Atmospheric Observations: The Stochastic Time-Inverted Lagrangian Transport (STILT) model, *Manuscript*, 2002.

Marland, G., T.A. Boden, A.L. Brenkert, R.J. Andres, and J.G.J. Olivier, CO2 from fossil fuel burning: Updates on the magnitude, distribution, and uncertainty of emission estimates., in *Fifth International Carbon Dioxide Conference*, pp. 4, Cairns, Queensland, Australia, 1997.

Masarie, K.A., and P.P. Tans, Extension and integration of atmospheric carbon dioxide data into a globally consistent measurement record, *Journal of Geophysical Research*, *100*, 11593-11610, 1995.

Nakazawa, T., K. Miyashita, S. Aoki, and M. Tanaka, Temporal and spatial variations of upper tropospheric and lower stratospheric carbon dioxide, *Tellus*, *43B*, 106-117, 1991.

Novelli, P.C., L.P. Steele, and P.P. Tans, Mixing ratios of carbon monoxide in the troposphere, *Journal of Geophysical Research*, *97* (D18), 20,731-20,750, 1992.

Novelli, P.C., K.A. Masarie, and P.M. Lang, Distributions and recent changes of carbon monoxide in the lower troposphere, *Journal of Geophysical Research*, *103* (D15), 19015-19033, 1998.

Potosnak, M.J., S.C. Wofsy, A.S. Denning , T.J. Conway, P.C. Novelli, and D.H. Barnes, Influence of biotic exchange and combustion sources on atmospheric CO_2 concentrations in New England from observations at a forest flux tower, *Journal of Geophysical Research*, *104* (D8), 9561-9569, 1999.

Stephens, B.B., S.C. Wofsy, R.F. Keeling, P.P. Tans, and M.J. Potosnak, The CO_2 budget and rectification airborne study: strategies for measuring rectifiers and regional fluxes, in *Inverse methods in global biogeochemical cycles*, edited by P. Kasibhatla, M. Heimann, P. Rayner, N. Mahowald, R.G. Prinn, and D.E. Hartley, pp. 311-324, American Geophysical Union, Washington, D.C., 1999.

Stull, R.B., *An introduction to boundary layer meteorology*, 666 pp., Kluwer, Dordrecht, The Netherlands, 1988.

Tans, P.P., I.Y. Fung, and T. Takashi, Observational constraints on the global atmospheric CO_2 budget, *Science*, *247*, 1431-1438, 1990.

Wei, W.W.S., *Time series analysis*, Addison-Wesley, 1989.

Wofsy, S.C., and R.C. Harris, The North American Carbon Program (NACP). Report of the NACP Committee of the U.S. Interagency Carbon Cycle Science Program., Washington, DC: US Global Change Research Program, 2002.

Zhao, C.L., P.P. Tans, and K.W. Thoning, A high precision manometric system for absolute calibrations of CO2 in dry air, *Journal of Geophysical Research*, *102* (D5), 5885-5894, 1997.

C. Gerbig, J. C. Lin, S. C. Wofsy, B. C. Daube, and A. E. Andrews[1], Dept. of Earth and Planetary Sciences and Division of Engineering and Applied Sciences, Harvard University, Cambridge, MA 02138. (chg@io.harvard.edu; jcl@io.harvard.edu; Steven_Wofsy@harvard.edu; bcd@io.harvard.edu; andrews@maia.gsfc.nasa.gov)

B. B. Stephens[2] and P. S. Bakwin, Climate Monitoring and Diagnostic Laboratory, National Oceanic and Atmospheric Administration, Boulder, CO 80305. (stephens@ucar.edu; pbakwin@cmdl.noaa.gov)

A. Grainger, Dept. of Atmospheric Sciences, University of North Dakota, Grand Forks, ND (grainger@aero.und.edu)

[1]Now at NASA Goddard Space Flight Center, Greenbelt, Maryland.

[2]Now at Research Aviation Facility, National Center for Atmospheric Research, Boulder, CO.

Figure 1. Schematic diagram of the data-analysis framework.

Figure 2. Flight routes of the Citation during the COBRA experiment in August 2000, comprising of northern survey flights (dark gray line), southern survey flights (dark gray dotted line), and regional airmass following flights (light gray lines).

Figure 3. Measured CO_2 and CO distribution as a function of altitude and longitude for the northern (a and b) and the southern transect (c and d), and Vegetation Condition Index (from NESDIS) for August 20, 2000 (e) and for August 22, 1999 (f); approximate flight tracks are superimposed. To interpolate the tracer data in altitude and longitude between the measurement locations, the squared inverse of the distance was used as weighting, with the distance measured in units of 500 m vertical and degree longitude horizontal (aspect ratio 1/200). Tracer data from different days and different times of the day were used for the cross-sections (see Table 1).

Figure 4. Profiles of CO_2 and H_2O collected around 15:00 local time over Duluth, MN (left). Profiles of the standard deviation of the departure from the mixed layer average CO_2 (right). Afternoon values are less variable (filled circles and solid lines) than morning/noon values (stars and dashed line). A distinct increase in variability at the upper 20% of the mixed layer is due to intermittent entrainment of air from the residual layer or free troposphere.

Figure 5. Total representativeness error of mixed layer averaged CO_2 mixing ratios (combined measurement uncertainty and representativeness error) plotted against the horizontal dimension of the region. Vertical bars indicate the 5-95% range.

Figure 6. ROM domain covering most of North America. Open circles indicate the subdomain for which EDAS winds where used. The starting locations for the particles along the flight track are indicated by the thick black lines. The gray scale indicates the number of particles ending in a particular grid cell after 15 days, or leaving the domain to the west.

Figure 7. Schematic diagram of key levels in an active cloud, after [*Stull*, 1988]. Virtual potential temperature profile is shown for environment and in-cloud air. Convective available potential energy is proportional to the shaded area.

Figure 8. Measurements in the western boundary area plotted against values predicted by the statistical models for CO_2 (left) and for CO (right). Black symbols represent surface data, and light gray symbols represent data above 300 m (airborne and high elevation station data).

Figure 9. Footprints for mixed layer receptors, integrated over the last two days prior to the measurements, calculated for the non-convective case for the northern (a) and the southern survey (b). Colors indicate The different pixel sizes are a result of the dynamic

grid resolution. The square with an edge length of 1 degree over the Atlantic Ocean is shown as reference.

Figure 10. Spatially integrated surface influence for mixed layer receptors as a function of time before arrival at the flight track, for the northern (solid symbols) and the southern transect (open symbols). Results for the convective case are shown as solid lines, and for the non-convective case as dashed lines.

Figure 11. Combustion signals for CO and CO_2 along the northern survey. CO fossil fuel signal ΔCO_{comb} (a and b) after Eq. 12, CO fossil fuel signal $\Delta CO_{ff,inv}$ (c and d) calculated by ROM using the emission inventory, and CO_2 combustion signal after Eq. 11, using measured CO and CO_2:CO emission ratio (e and f). Left column (a, c, and e) shows results for the non-convective case, right column (b, d, and f) for the convective case.

Figure 12. CO_2 vegetation signals after Eq. 9, for the northern survey (a) and the southern survey (b), both for the non-convective case.

Figure 13. 24-hour averages of NEE from forests and croplands based on the upscaling of AmeriFlux data for three consecutive days preceding the measurements. The top and bottom row show results using scaling factors constrained by the northern and the southern survey, respectively.

Figure 14. Modeled vegetation CO_2 signal for the non-convective case (a,b) and for the convective case (c,d). Left column (a and c) shows results for the northern survey, right column (b and d) for the southern survey.

Figure A1. Differences in mixed layer averaged CO_2 measured at different locations (i,j) within a three-hour period, plotted against the spatial distance of the measurement locations.

Figure A2. Robust variogram estimates (filled squares) for different distance bins. Points are robust variogram estimates with one observation deleted. Vertical bars represent 1 σ errors derived from the Jackknife delete-1 statistics. The solid line represents a power variogram model fitted to the robust variogram estimates, and the dashed lines correspond to the 95% confidence interval for the variogram fit.

Figure A3. Result of a spatial simulation for a 20×20 grid element area. A mean of 365 ppm was assumed, and the spatial variability is determined by the fitted power variogram.

Table 1: Dates and locations of flights used to create cross-sections for transcontinental surveys

Date, Start-End [GMT]	Regions over flown (State)	Survey
Aug 6, 19:58-20:47	ID, WY, CO	southern
Aug 8, 14:31-16:38	CO, KS, MO	southern
Aug 9, 13:30-15:19	KS, MO, IL, IN	southern
Aug 9, 16:30-18:03	IN, OH, PA	southern
Aug 9, 18:52-20:25	PA, NY, MA	southern
Aug 11, 12:06-14:29	MA, NH, ME	southern
Aug 18, 18:19-20:53	ME, NH, MA	northern
Aug 19, 12:17-14:42	MA, NH, VT, NY, Ontario (CAN), MI	northern
Aug 19, 15:28-16:28	MI, WI	northern
Aug 19, 17:58-19:50	WI, MN, ND	northern

Table 2: Data used in the climatology for the boundary condition (CO and CO_2), together with corresponding time periods, locations and data source. Acronyms for data sources are: CMDL: NOAA Climate Monitoring and Diagnostics Laboratory, Carbon Cycle Group (Cooperative Air Sampling Network); GTE, Global Tropospheric Experiment, from NASA Langley Research Center Atmospheric Sciences Data Center (http://cloud1.arc.nasa.gov/index.html); ESPO, NASA Ames Research Center Earth Science Projects Office Missions (http://espoarchive.nasa.gov/archive/); CODIAC: Joint Office for Science Support (JOSS) UCAR Data Management Center (http://www.joss.ucar.edu/codiac/).

Campaign/platform	Date (start-end) [M/D/Y]	Lat. [°N]	Lon. [°W]	Alt. [km]	Tracer	Source
Barrow (BRW)	9/18/1980-5/19/2001	71	156	0	CO,CO_2	CMDL
Cold Bay (CBA)	9/18/1980-5/28/2001	55	162	0	CO,CO_2	CMDL
Cape Kumukahi (KUM)	9/16/1980-5/29/2001	20	154	0	CO,CO_2	CMDL
Mauna Loa (MLO)	9/19/1980-5/30/2001	20	155	3	CO,CO_2	CMDL
Niwot Ridge (NWR)	9/18/1980-5/29/2001	40	105	3	CO	CMDL
commercial B747	1/1/1984-12/8/1985	20-61	149-220	7-11	CO_2	[*Nakazawa et al.*, 1991]
PEM-West-A (DC8)	10/18/1991-10/21/1991	16-34	136-180	0-12	CO_2	GTE
AASE-2	1/14/1992-3/13/1992	10-90	27-347	1-12	CO_2	ESPO
PEM-West-B (DC8)	2/8/1994-3/14/1994	21-61	122-180	0-10	CO,CO_2	GTE
ASHOE/MAESA	3/18/1994-10/29/1994	20-22	157-159	9-13	CO,CO_2	ESPO
MAPS Satellite	4/24/1994-10/25/1994	10-55	100-180	8-8	CO	ESPO
ACE-1	10/31/1995-12/23/1995	10-76	123-160	0-8	CO,CO_2	CODIAC
TOTE/VOTE	12/8/1995-2/19/1996	10-82	119-180	1-13	CO,CO_2	ESPO
SUCCESS	5/11/1996-5/14/1996	38-46	123-127	3-12	CO,CO_2	ESPO
PEM-Tropics A (P3)	8/18/1996-8/31/1996	10-37	123-165	0-8	CO,CO_2	GTE
PEM-Tropics A (DC8)	8/30/1996-10/6/1996	10-45	123-158	0-10	CO,CO_2	GTE
STRAT	10/26/1995-12/12/1996	20-37	121-161	9-13	CO,CO_2	ESPO
Carr (CO)	7/17/1995-1/1/1997	41-41	105-105	8	CO,CO_2	CMDL
POLARIS	6/26/1997-9/23/1997	20-66	145-159	0-12	CO,CO_2	ESPO
PEM-Tropics B (P3)	3/11/1999-4/9/1999	10-33	119-158	0-7	CO,CO_2	GTE
PEM-Tropics B (DC8)	3/6/1999-4/18/1999	10-33	105-164	0-12	CO,CO_2	GTE

Table 3: AmeriFlux sites used for parameterization of NEE for different vegetation types

Site	Vegetation type (IGBP classification)	Vegetation type (simplified)	Vegetation (AmeriFlux-description)
Duke Forest (NC)	Evergreen needleleaf forest	Forest	Even-aged loblolly pine plantation
Harvard Forest (MA)	Deciduous broadleaf forest	Forest	Temperate deciduous forest
Howland (MN)	Mixed forest	Forest	Deciduous needle forest, Boreal/northern hardwood ecotone, old coniferous
Walker Branch (TN)	Deciduous broadleaf forest	Forest	Mixed-species, broad-leaved forest, deciduous forest
Willow Creek (WI)	Deciduous broadleaf forest	Forest	Sugar maple-basswood forest, with some green ash and red oak
WLEF Wisconsin Tall Tower (WI)	Mixed forest	Forest	Temperate/Boreal forest, lowland and wetland forest
Little Washita (OK)	Woody savannas	Shrubland	Rangeland
Shidler (OK)	Grasslands	Shrubland	Native tall grass prairie warm season C4
Sky Oaks - Old Stand (CA)	Open shrubland	Shrubland	Chaparral (Mediterranean-type ecosystems)
Sky Oaks - Young Stand (CA)	Open shrubland	Shrubland	Chaparral (Mediterranean-type ecosystems)
Bondville (IL)	Croplands	Cropland	Annual rotation between Corn (C4) - 2001, Soybeans (C3) - 2000

Table 4: Relative influence and NEE signal from different vegetation classes, for mixed layer receptors, averaged over the respective survey (non-convective case). Initial NEE signal refers to upscaling of Tower Fluxes using the simplified vegetation classification; optimized NEE signals use the respective scaling factors to match measured vegetation signals.

	Relative influence		**Initial NEE signal [ppm]**		**Optimized NEE signal [ppm]**	
Survey→ Vegetation↓	north	south	north	south	north	south
Forests	45%	28%	-7.7	-1.6	- 6.5	- 0.6
Water bodies	25%	31%	-0.1	-0.2	n.a.	n.a.
Shrublands	16%	31%	-1.4	-0.4	n.a.	n.a.
Croplands	12%	12%	-8.1	-5.0	- 2.5	- 0.4
Wetlands	2%	<1%	n.a.	n.a.	n.a.	n.a.

Table 5: Scaling factors for net biosphere-atmosphere exchange flux, optimized to match observed vegetation signals $\Delta CO_{2,veg}$. STILT was run with upper-limit convection

and without convection. Uncertainty ranges are obtained by repeating the optimization with added/subtracted uncertainty in $\Delta CO_{2,veg}$.

	Strong convective fluxes		**Zero convective fluxes**	
Region	**Forest**	**Crop**	**Forest**	**Crop**
North	1.18±0.15	0.60±0.15	0.85±0.15	0.31±0.04
North-East	0.97±0.20	0.73±0.23	0.70±0.15	0.18±0.25
South	0.48±0.52	0.27±0.39	0.41±0.28	0.07±0.22

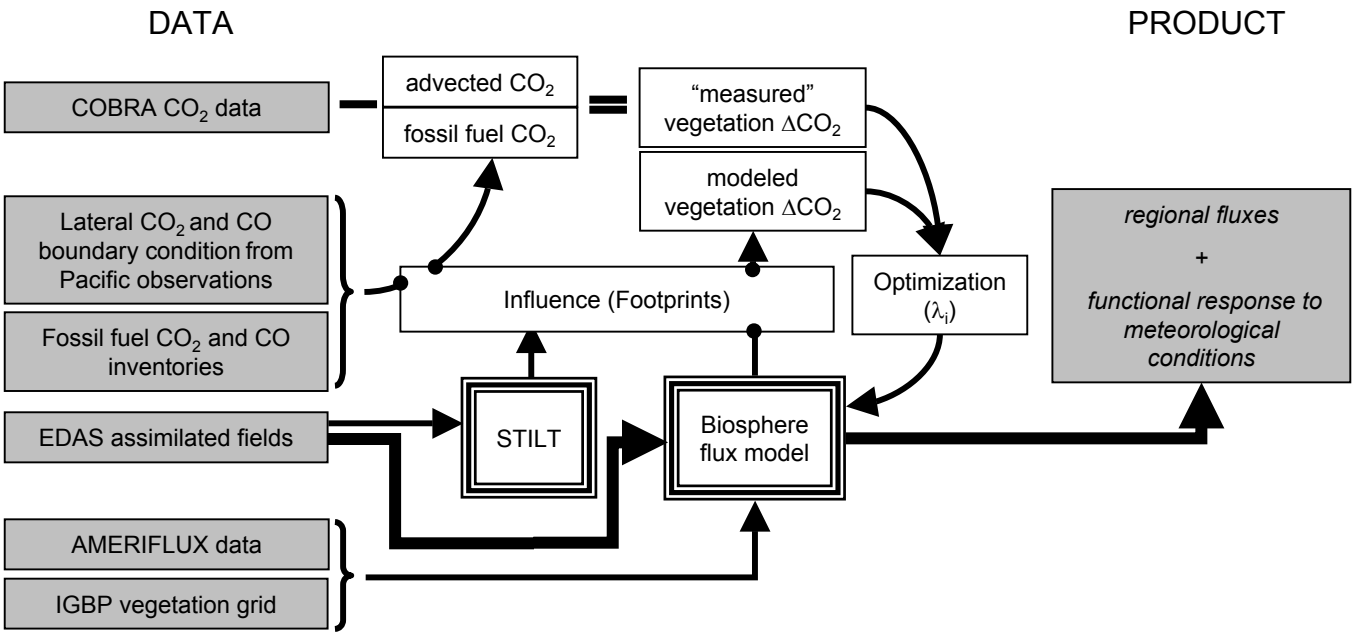

Figure 1. Schematic diagram of the data-analysis framework.

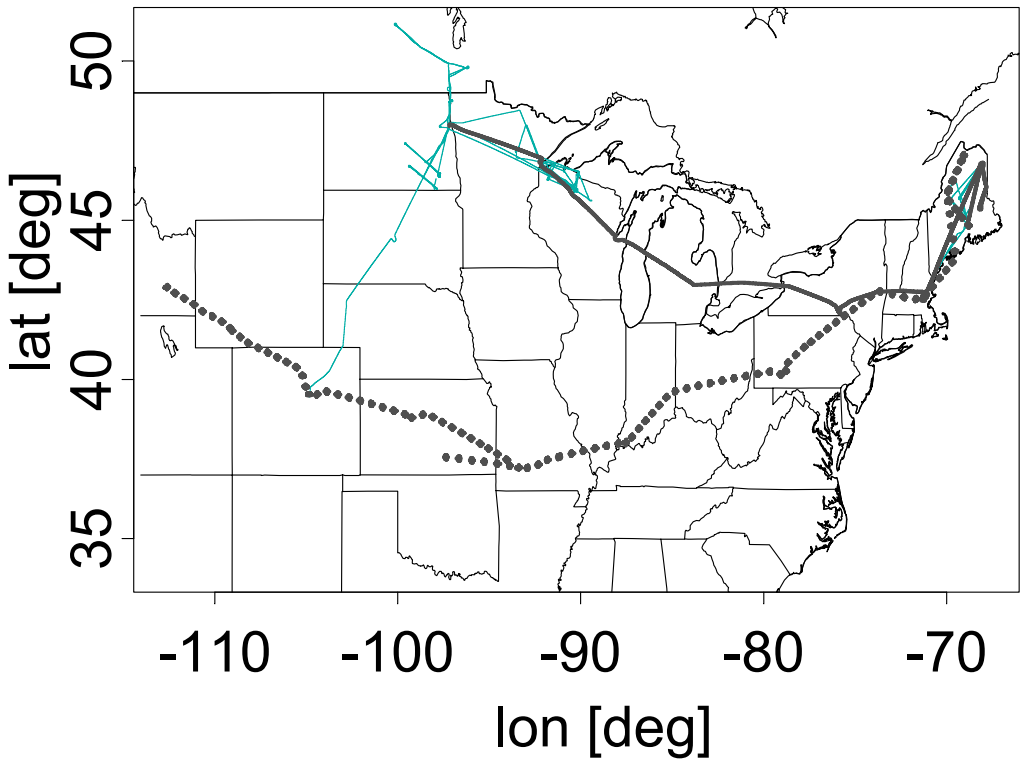

Figure 2. Flight routes of the Citation during the COBRA experiment in August 2000, comprising of northern survey flights (dark gray line), southern survey flights (dark gray dotted line), and regional airmass following flights (light gray lines).

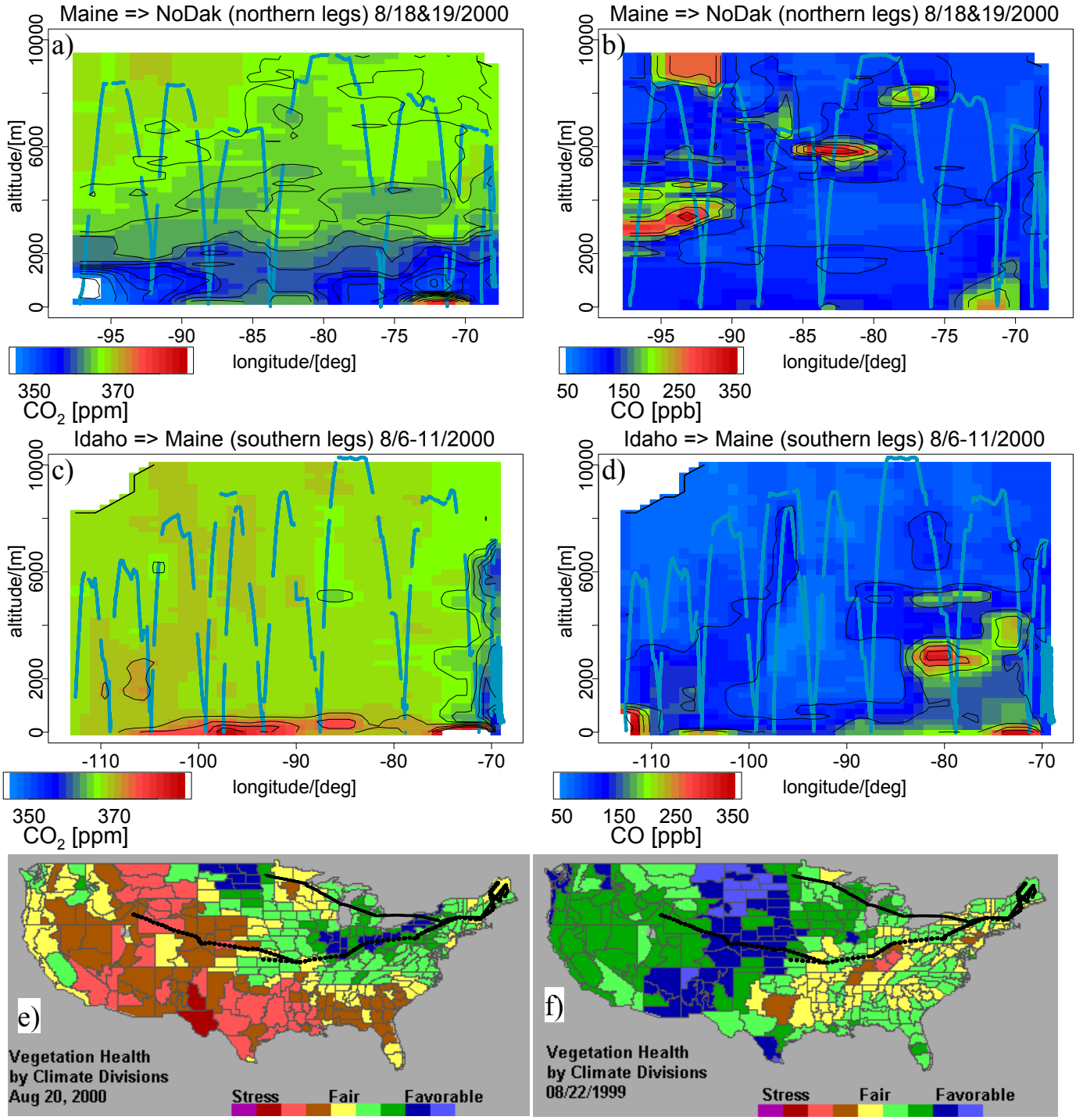

Figure 3. Measured CO_2 and CO distribution as a function of altitude and longitude for the northern (a and b) and the southern transect (c and d), and Vegetation Condition Index (from NESDIS) for August 20, 2000 (e) and for August 22, 1999 (f); approximate flight tracks are superimposed. To interpolate the tracer data in altitude and longitude between the measurement locations, the squared inverse of the distance was used as weighting, with the distance measured in units of 500 m vertical and degree longitude horizontal (aspect ratio 1/200). Tracer data from different days and different times of the day were used for the cross-sections (see Table 1).

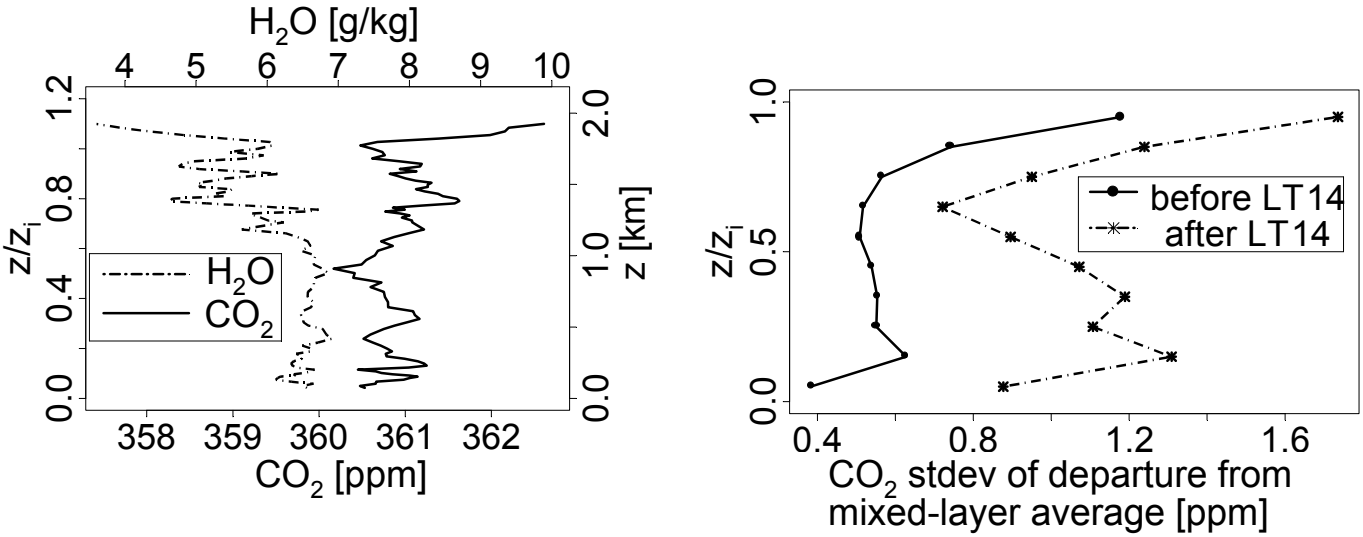

Figure 4. Profiles of CO_2 and H_2O collected around 15:00 local time over Duluth, MN (left). Profiles of the standard deviation of the departure from the mixed layer average CO_2 (right). Afternoon values are less variable (filled circles and solid lines) than morning/noon values (stars and dashed line). A distinct increase in variability at the upper 20% of the mixed layer is due to intermittent entrainment of air from the residual layer or free troposphere.

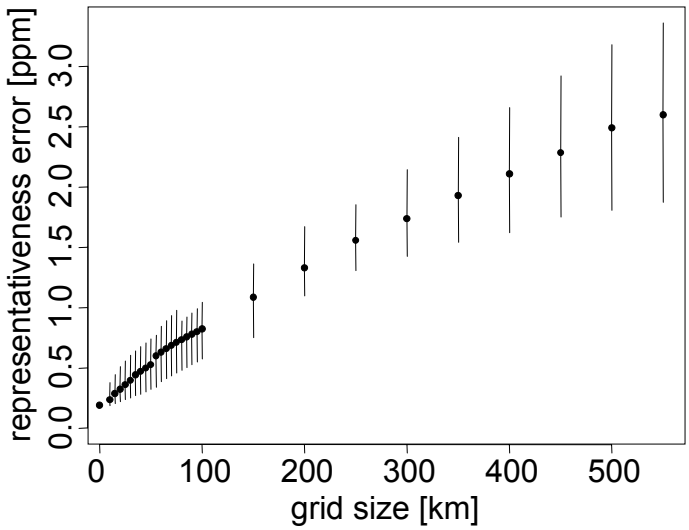

Figure 5. Total representativeness error of mixed layer averaged CO_2 mixing ratios (combined measurement uncertainty and representativeness error) plotted against the horizontal dimension of the region. Vertical bars indicate the 5-95% range.

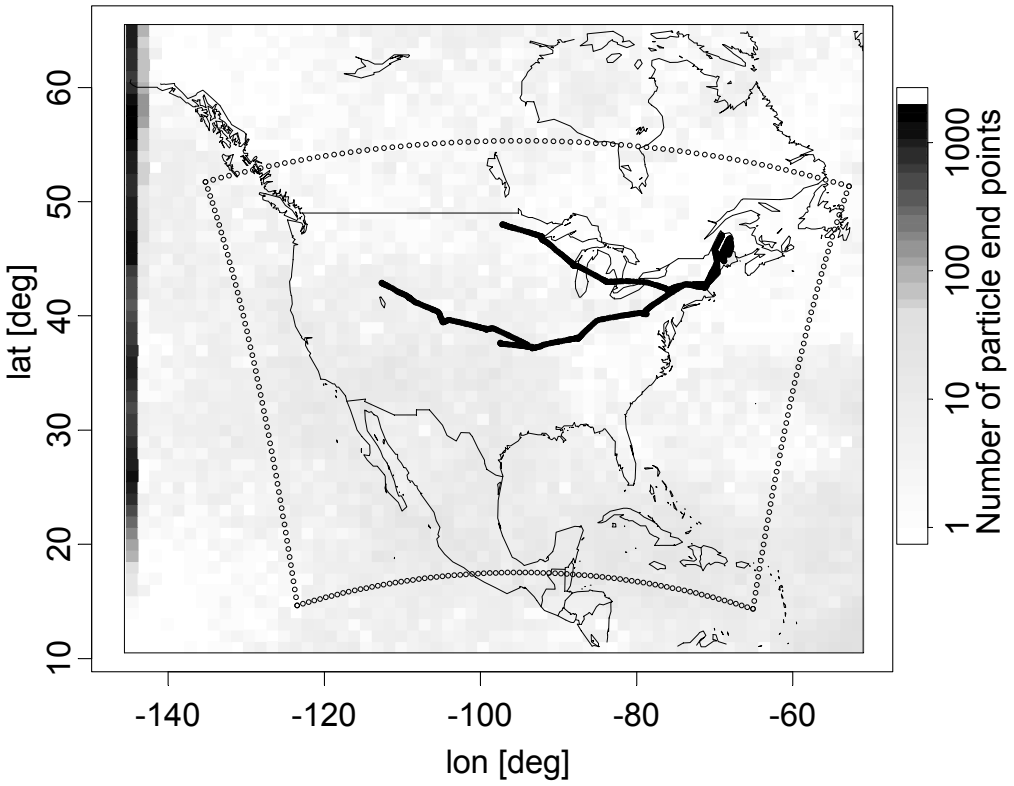

Figure 6. ROM domain covering most of North America. Open circles indicate the subdomain for which EDAS winds where used. The starting locations for the particles along the flight track are indicated by the thick black lines. The gray scale indicates the number of particles ending in a particular grid cell after 15 days, or leaving the domain to the west.

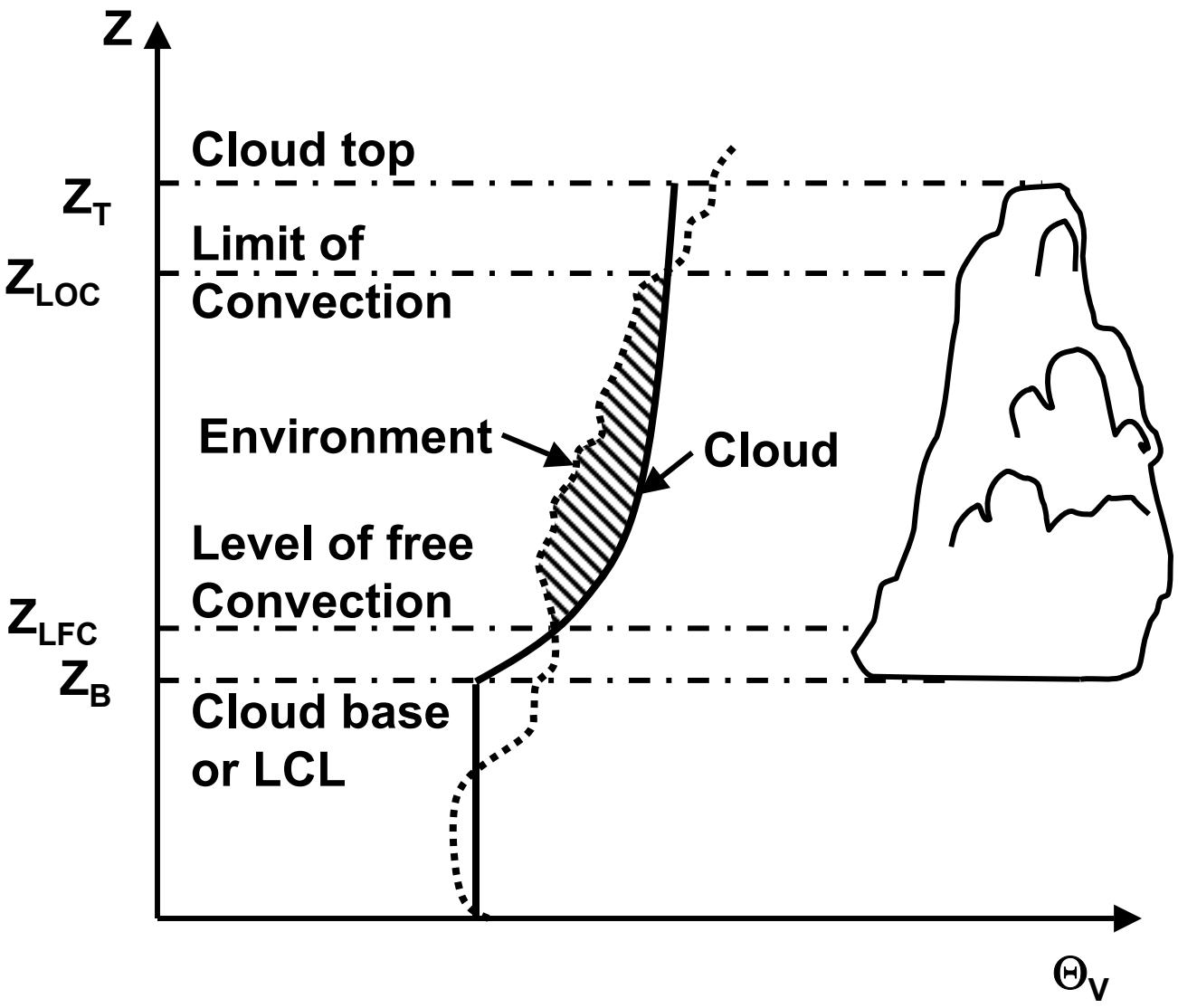

Figure 7. Schematic diagram of key levels in an active cloud, after [*Stull*, 1988]. Virtual potential temperature profile is shown for environment and in-cloud air. Convective available potential energy is proportional to the shaded area.

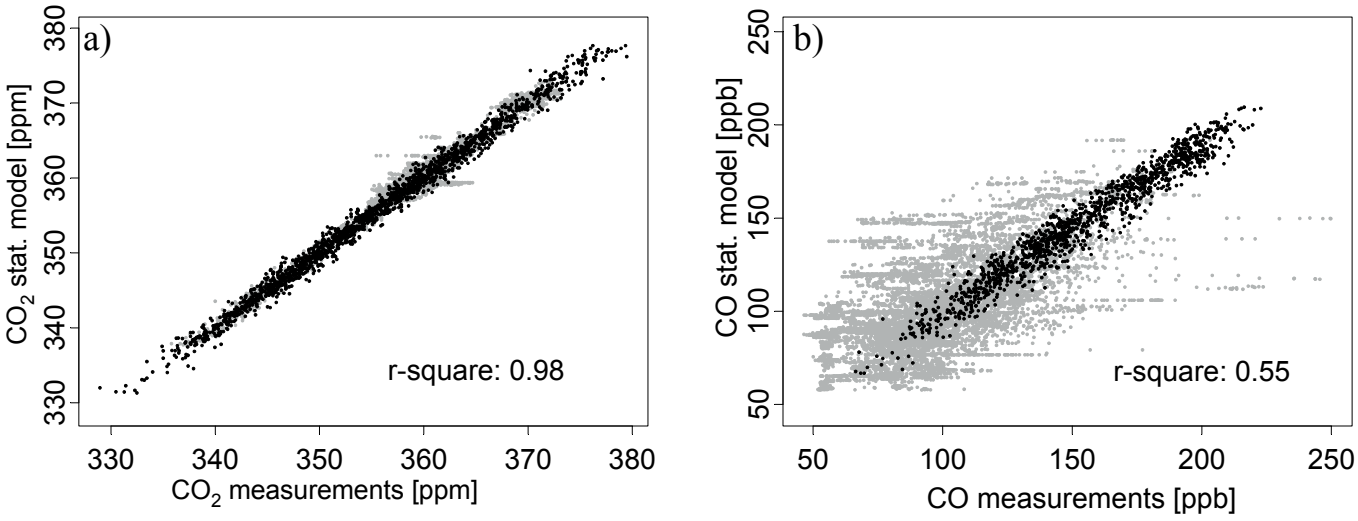

Figure 8. Measurements in the western boundary area plotted against values predicted by the statistical models for CO_2 (left) and for CO (right). Black symbols represent surface data, and light gray symbols represent data above 300 m (airborne and high elevation station data).

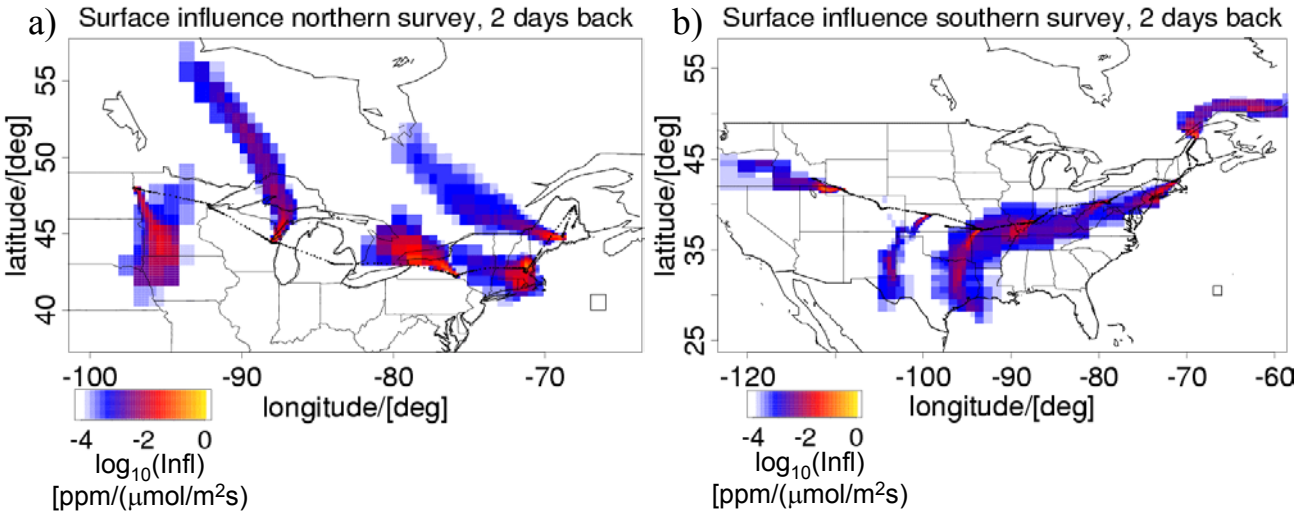

Figure 9. Footprints for mixed layer receptors, integrated over the last two days prior to the measurements, calculated for the non-convective case for the northern (a) and the southern survey (b). The different pixel sizes are a result of the dynamic grid resolution. The square with an edge length of 1 degree over the Atlantic Ocean is shown as reference.

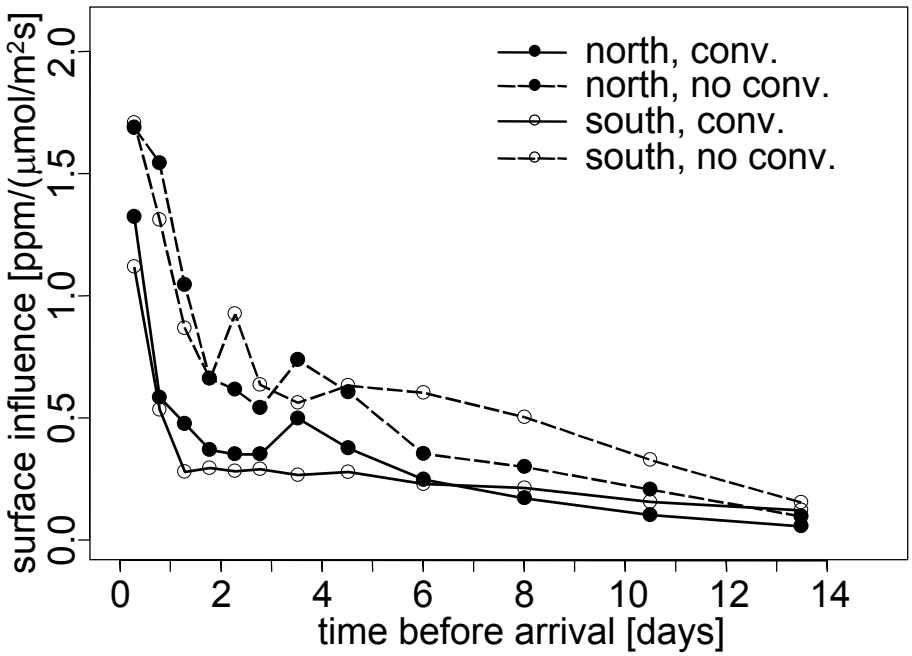

Figure 10. Spatially integrated surface influence for mixed layer receptors as a function of time before arrival at the flight track, for the northern (solid symbols) and the southern transect (open symbols). Results for the convective case are shown as solid lines, and for the non-convective case as dashed lines.

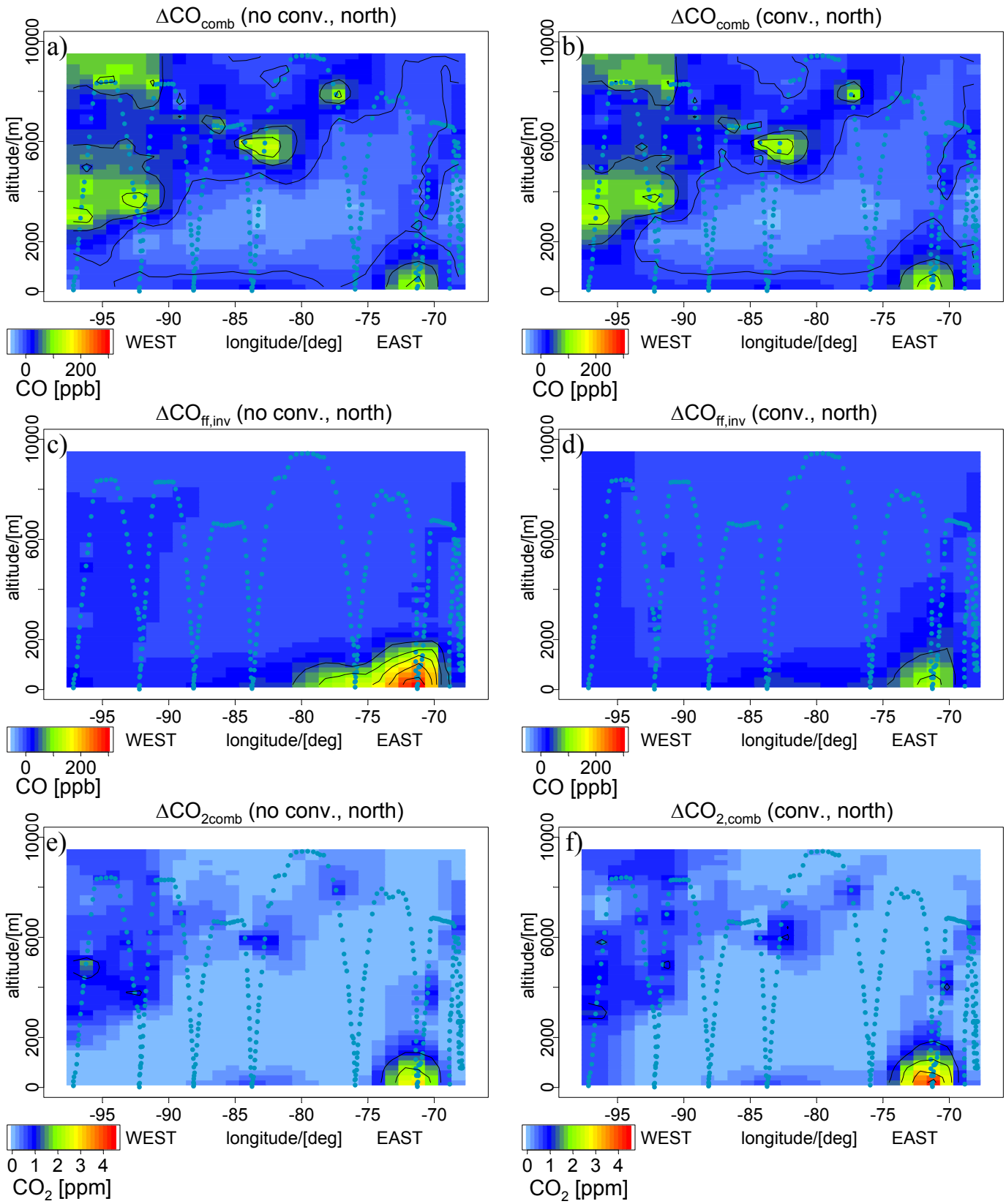

Figure 11. Combustion signals for CO and CO_2 along the northern survey. CO fossil fuel signal $CO_{ff,meas}$ (a and b) after Eq. 10, CO fossil fuel signal $CO_{ff,inv}$ (c and d) calculated by ROM using the emission inventory, and CO_2 combustion signal after Eq. 11, using measured CO and CO_2:CO emission ratio (e and f). Left column (a, c, and e) shows results for the non-convective case, right column (b, d, and f) for the convective case.

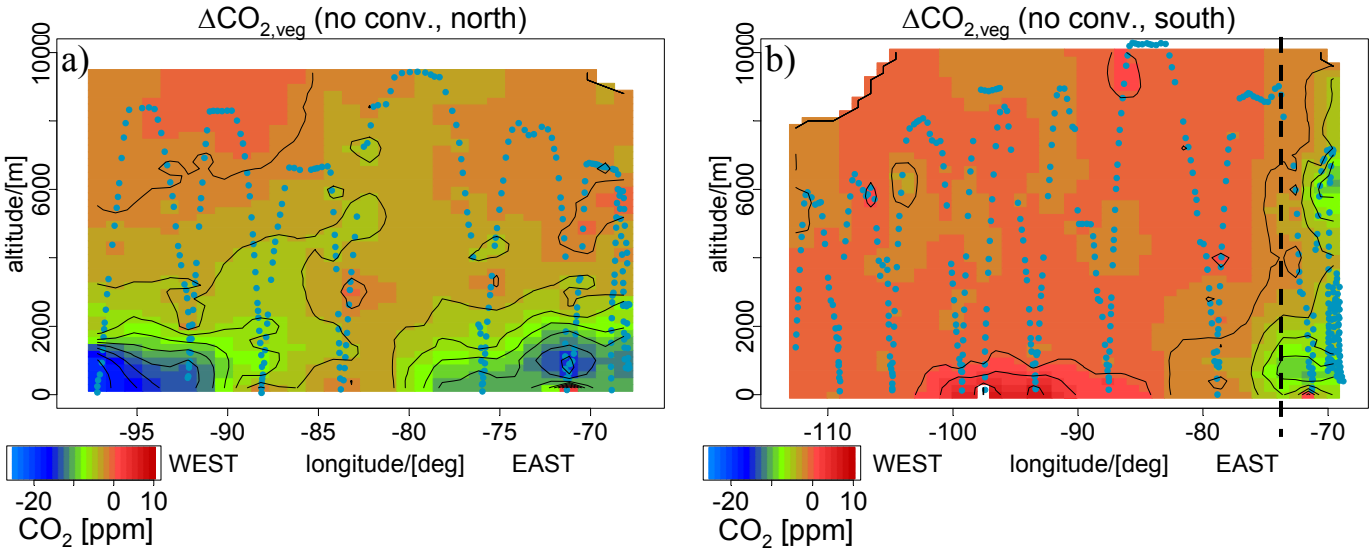

Figure 12. CO_2 vegetation signals after Eq. 9, for the northern survey (a) and the southern survey (b), both for the non-convective case. The vertical dashed line in b) marks the eastern end of the data used in the optimization for the southern survey.

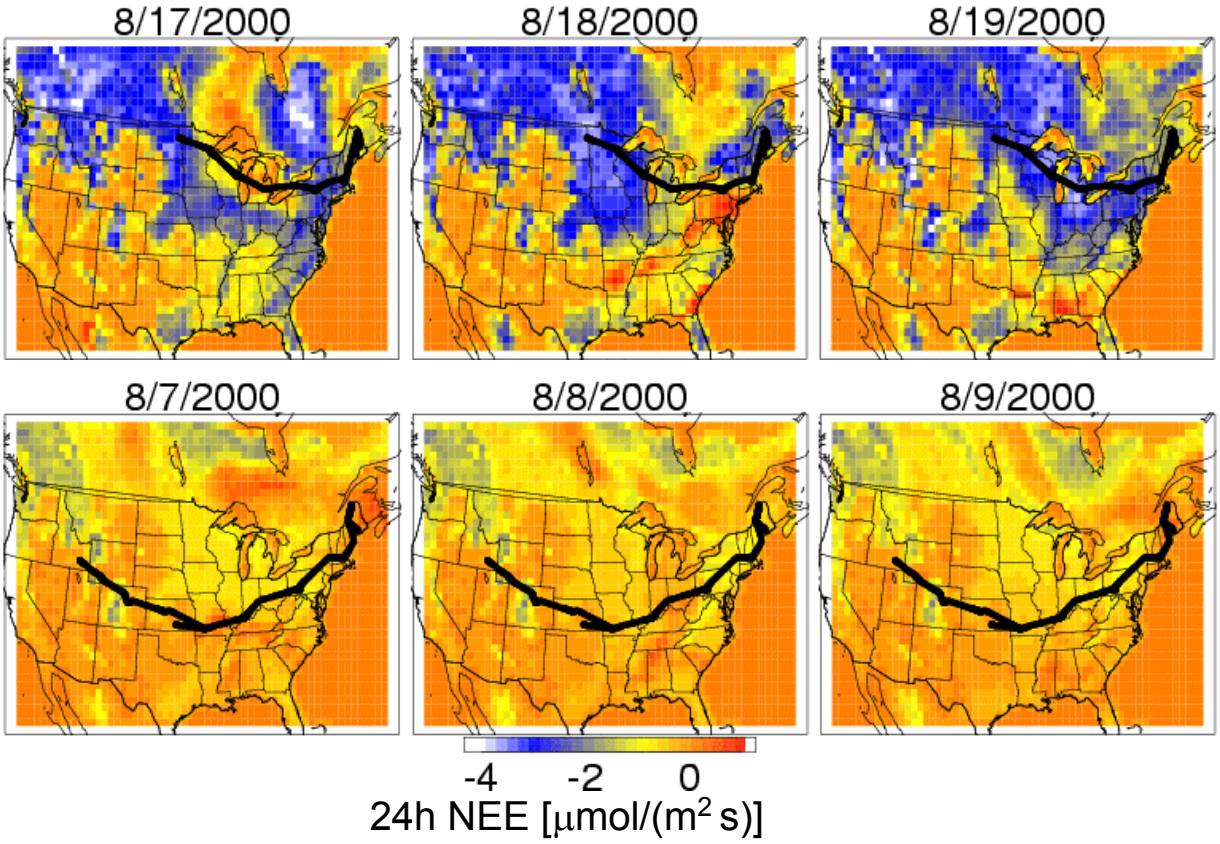

Figure 13. 24-hour averages of NEE from forests and croplands based on the upscaling of AmeriFlux data for three consecutive days preceding the measurements. The top and bottom row show results using scaling factors constrained by the northern and the southern survey, respectively.

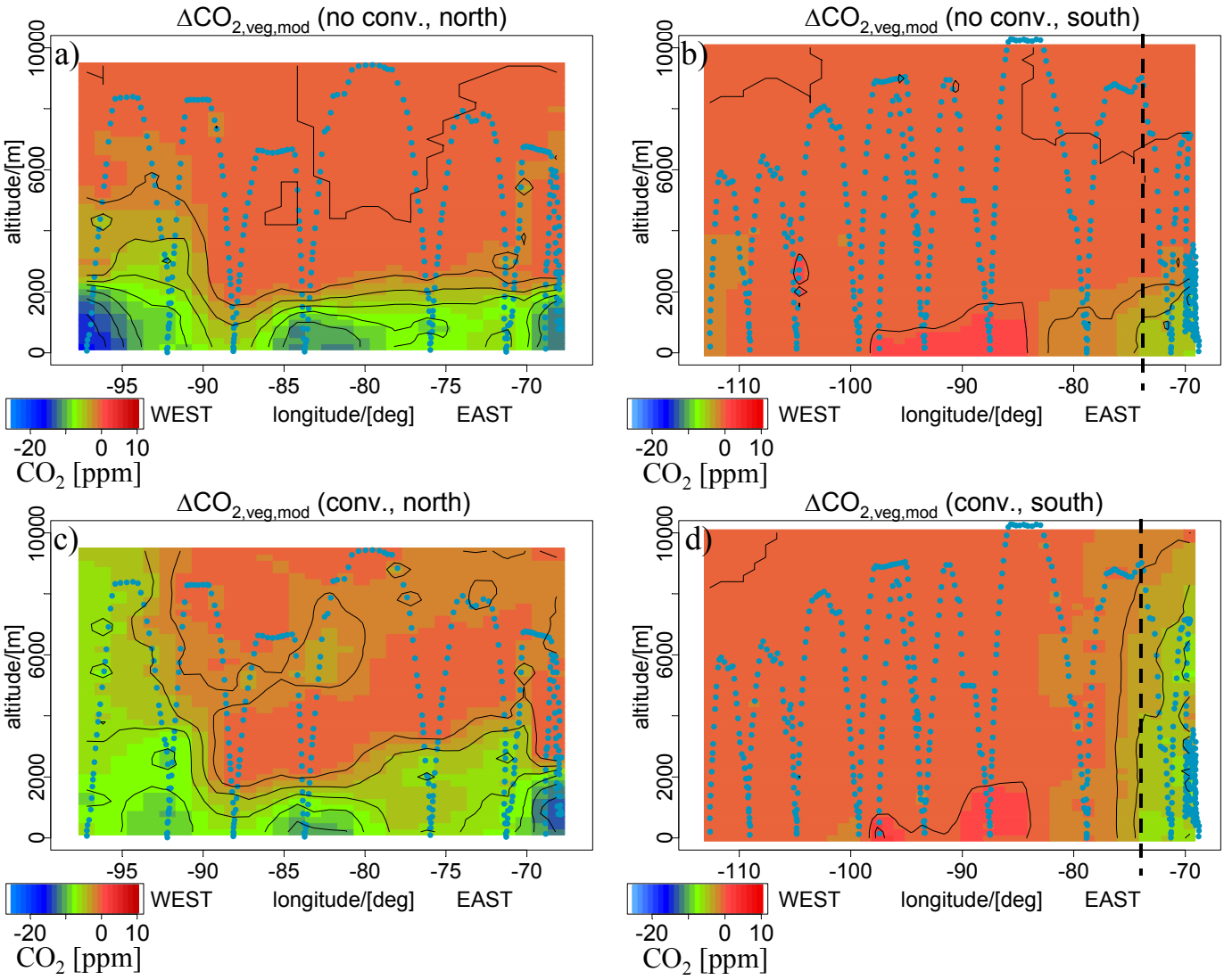

Figure 14. Modeled vegetation CO_2 signal for the non-convective case (a,b) and for the convective case (c,d). Left column (a and c) shows results for the northern survey, right column (b and d) for the southern survey. Left of the vertical dashed lines in b) and d) the southern survey scaling factors are used, to the right of these lines different scaling factors were applied.

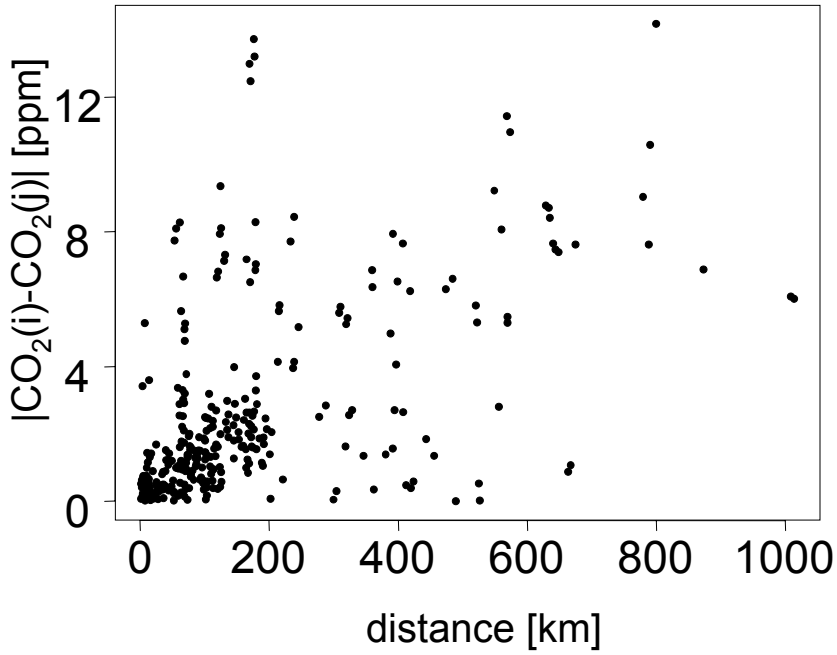

Figure A1. Differences in mixed layer averaged CO_2 measured at different locations (i,j) within a three hour period, plotted against the spatial distance of the measurement locations.

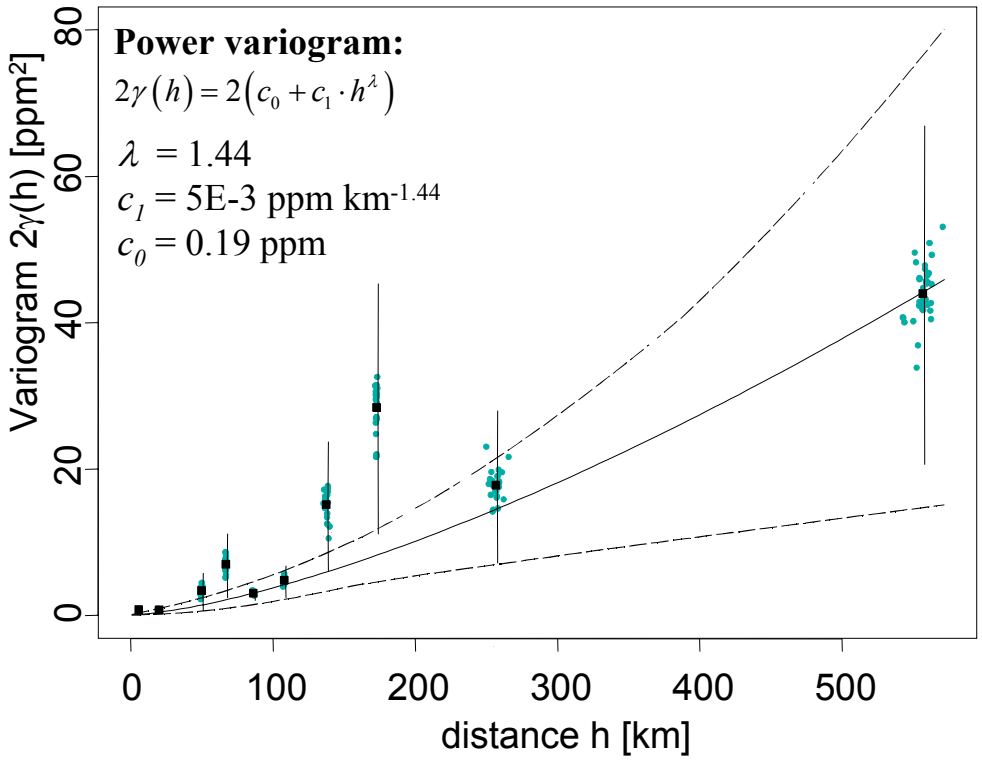

Figure A2. Robust variogram estimates (filled squares) for different distance bins. Points are robust variogram estimates with one observation deleted. Vertical bars represent 1 σ errors derived from the Jackknife delete-1 statistics. The solid line represents a power variogram model fitted to the robust variogram estimates, and the dashed lines correspond to the 95% confidence interval for the variogram fit.

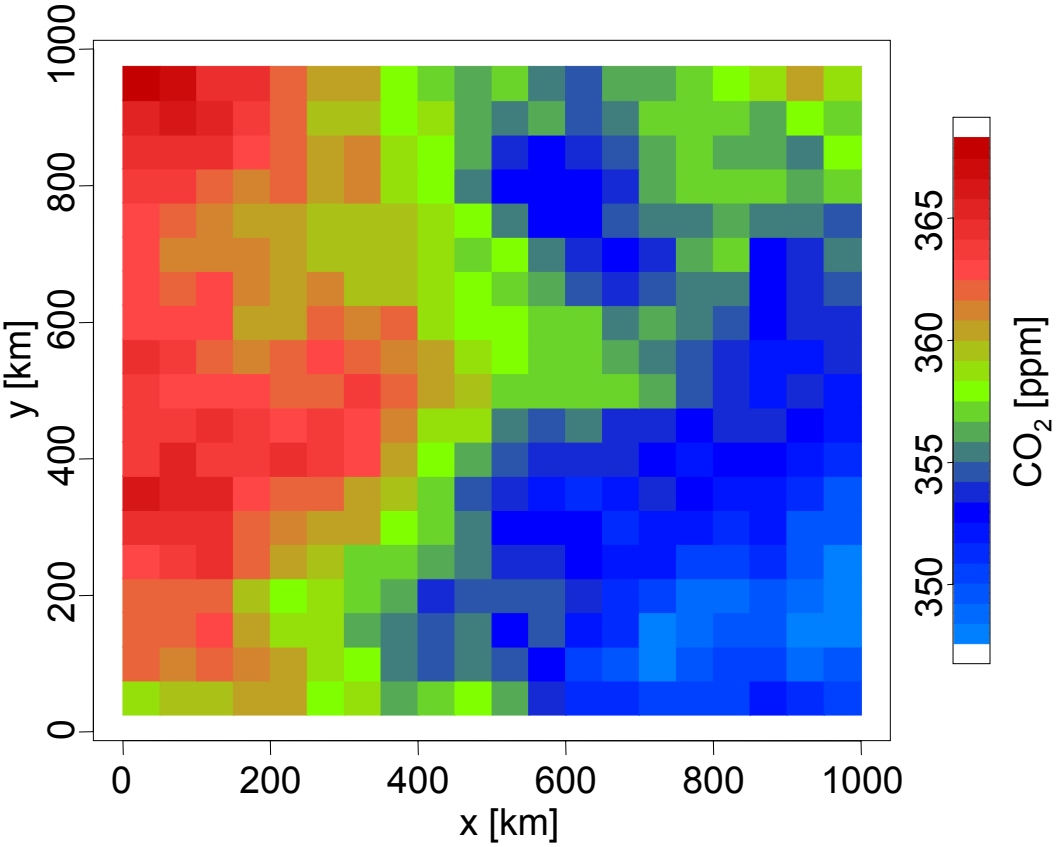

Figure A3. Result of a spatial simulation for a 20*20 grid element area. A mean of 365 ppm was assumed, and the spatial variability is determined by the fitted power variogram.